

2000

Solid-State Sensors, Actuators, and Microsystems Workshop

Late News Poster Session Supplemental Digest

Table of Contents

Author Index

Copyright

www.hh2000.org



Sponsored by the
Transducer Research Foundation, Inc.
Additional support provided:
Defense Advanced Research Projects Agency

Hilton Head Workshop
June 4 - 8, 2000 • Hilton Head, South Carolina
Editors: Martin W. Schmidt & Luc Bousse

TRF Catalog Number: 00TRF-0001
Library of Congress Control Number: 00-102144
ISBN Number: 0-9640024-3-4
ISSN 1539-2058 (Print) • ISSN: 1539-204X (Electronic)
DOI 10.31438/trf.hh2000A.0

2000

Solid-State Sensors, Actuators, and Microsystems Workshop

Hilton Head Island, South Carolina • June 4 - 8, 2000

All opinions expressed in this digest are those of the authors and are not binding on Transducer Research Foundation, Inc.

Copies of available volumes of this digest may be obtained from the Transducer Research Foundation, Inc., c/o 307 Laurel Street, San Diego, California 92101-1630 USA (+1-619-232-9499)

Copyright and Reprint Permission: Abstracting is permitted with credit to the source. Libraries are permitted to photocopy beyond the limit of U.S. copyright law for private use of patrons those articles in this volume that carry a code at the bottom of the first page, provided the per-copy fee indicated in the code is paid through Copyright Clearance Center, 222 Rosewood Drive, Danvers, MA 01923. For other copying, reprint or republication permission, contact Transducer Research Foundation, Inc., c/o 307 Laurel Street, San Diego, California 92101-1630 USA, info@transducer-research-foundation.org. All rights reserved. Copyright ©2000 by the Transducer Research Foundation, Inc. Personal use of this material is permitted. However, permission to reprint/republish this material for advertising or promotional purposes or for creating new collective works for resale or redistribution to servers or lists, or to reuse any copyrighted component of this work in other works must be obtained from the Transducer Research Foundation, Inc.

TRF Catalog Number: 00TRF-0001

Library of Congress Control Number: 00-102144

ISBN Number: 0-9640024-3-4

ISSN 1539-2058 (Print) • ISSN: 1539-204X (Electronic)

DOI 10.31438/trf.hh2000A.0

This product contains Adobe Acrobat software. Copying this product's instructions and/or designs for use on future CD-ROMs or digital products is prohibited without written permission from The Printing House and Adobe Systems Incorporated. The Printing House or its suppliers are not liable for any direct, indirect, special, incidental, or consequential damages to your hardware or other software arising out of the use—or the inability to use—the material on this CD-ROM. This includes, but is not limited to, the loss of data or loss of profit. Adobe, Acrobat and the Acrobat logo are trademarks of Adobe Systems Incorporated or its subsidiaries and may be registered in certain jurisdictions.

If you have questions regarding the installation, please contact:



The Printing House

Phone: +1-608-873-4500

Hours: Monday through Friday, 8 am - 5 pm CST

E-mail: graphics@printinghouseinc.com

Solid-State Sensor and Actuator Workshop
June 4 – 8, 2000
Crowne Plaza Resort
Hilton Head Island, South Carolina

Late News Poster Session

Table of Contents

<i>Surface/Bulk Micromachined High Performance Silicon Micro-Gyroscope</i> D. Cho, S. Lee [†] , and S. Park [†] ; UC Berkeley, [†] Seoul National University	1
<i>Development of a Magnetic Flexible Membrane Micropump</i> M. Khoo, L.-H. Lu, and C. Liu; University of Illinois at Urbana-Champaign	3
<i>100% Foundry Compatible Packaging and Full Wafer Release/Die Separation Technique for Surface Micromachined Devices</i> A. Oliver and C. Matzke; Sandia National Laboratories	5
<i>Linearization and Analysis of Electrostatically Actuated MEMS 2D Optical Scanner</i> H. Toshiyoshi, W. Piyawattanametha, C.T. Chan, and M.C. Wu; UC Los Angeles	7
<i>Microinstrument for Transdermal, Woundpotential Measurements</i> E.V. Mukerjee, S.D. Collins, and R.L. Smith; UC Davis	9
<i>The Design-Fix for Fixed-Valve Micropumps</i> C.J. Morris and F.K. Forster; University of Washington	11
<i>Nozzle-Diffuser Based Micro Bubble Pump</i> J.-H. Tsai and L. Lin [†] ; University of Michigan, [†] UC Berkeley	13
<i>Ferromagnetic Micromechanical Magnetometers</i> J.W. Judy, H. Yang, N.Myung, P. Irazoqui-Pastor, M. Schwartz, K. Nobe, and K. Yang; UC Los Angeles	15
<i>A MEMS 2-D Scanner with Bonded Single-Crystalline Honeycomb Micromirror</i> P.R. Patterson, G.-D.J. Su, H. Toshiyoshi, and M.C. Wu; UC Los Angeles	17
<i>A Micromachined Resonant Magnetic Field Sensor</i> T.C. Leïchl�e, M. von Arx, and M.G. Allen; Georgia Tech	19
Author Index	21

TECHNICAL PAPERS

Solid-State Sensors, Actuators, and Microsystems Workshop

2000

**Hilton Head Island, South Carolina
June 4 - 8**

SURFACE/BULK MICROMACHINED HIGH PERFORMANCE SILICON MICRO-GYROSCOPE

Dong-il (Dan) Cho

Department of Mechanical Engineering, University of California, Berkeley
Berkeley, CA 94720, USA

Sangwoo Lee and Sangjun Park

School of Electrical Engineering and Computer Science, Seoul National University
Kwanak-gu, Seoul 151-742, Korea

ABSTRACT

A single-crystalline, single-wafer micro-gyroscope is fabricated using the Surface/Bulk Micromachining (SBM) process. The structural thickness of fabricated micro-gyroscope is 40 μm , and the sacrificial gap is 50 μm . For electrostatic actuation and capacitive sensing a new electrical isolation method, which uses sandwiched oxide, polysilicon and metal films, is developed. The measured noise equivalent random angle walk of the SBM fabricated gyroscope is $0.0025 \text{ }^\circ/\text{sec}/\sqrt{\text{Hz}}$. The output is measured to be linear up to $\pm 20 \text{ }^\circ/\text{sec}$.

INTRODUCTION

Increasing the structural thickness and using single-crystalline silicon to achieve improved performance for gyroscopes have been an important research topic in recent years. Many process techniques for fabricating High-Aspect Ratio Structures (HARS), such as the SOI [1], epi-poly [2], SOG [3], and SBM [4] processes have been developed. The epi-poly process can have problems of residual stress or stress gradient. The high cost and the residual stress resulting from the bonding process, as well as the footing phenomenon, are the main disadvantages for the SOI and SOG processes.

This paper presents a single-crystalline, single-wafer gyroscope fabricated using the SBM process. A new isolation method for electrostatic actuation and capacitive sensing is also developed in this paper.

EXPERIMENTAL DETAILS

The SBM technology utilizes standard (111) silicon wafers, and arbitrarily-shaped, released bulk-silicon structures can be fabricated in a single wafer. The SBM process yields very flat and smooth top and bottom surfaces as shown in Fig. 1. It is also free from the footing effects. We have fabricated structures ranging from 2-100 μm in thickness with a sacrificial gap of 2-100 μm . Note that the material properties are transversely isotropic on Si (111) planes, which is very desirable.

Several methods have been reported for electrical isolation of the single-crystalline silicon MEMS [4]-[7]. All of these processes have limitations for application to HARS, which for brevity are not explained in detail.

This paper develops a new oxide/polysilicon/metal triple film isolation method. The detailed process is shown in Fig. 2. In Fig. 2, it is assumed that a silicon microstructure is already fabricated. The isolation process starts with the oxidation of all exposed surfaces (Fig. 2(a)), followed by heavily-doped LPCVD polysilicon deposition (Fig. 2(b)). Since LPCVD polysilicon films have an excellent step coverage, they are deposited on all exposed surfaces. Then, an Al film is sputtered or evaporated (Fig. 2(c)). The

polysilicon films at the exposed bottom areas are then anisotropically etched away (Fig. 2(d)), using the top Al layer as the etch mask. Electrical isolation is obtained in this step. Figure 3 shows SEM photographs of an electrode fabricated by the SBM process and this triple film isolation technology.

A gyroscope fabricated using the SBM and triple film isolation method is shown in Fig. 4. The structural thickness is 40 μm , and the sacrificial gap is 50 μm . The overall size is 2.2 mm \times 3 mm. The driving and sensing modes of the gyroscope are decoupled, and the resonant frequencies of driving and sensing modes are 4.6 and 5.7 kHz, respectively. The total sensing capacitance is 3.12 pF.

RESULTS

Figure 5 shows the results when a 10 $^\circ/\text{sec}$, 11 Hz angular rate is applied. The test was performed in a 10 mTorr vacuum chamber. A 0.8 volt peak-to-peak sinusoidal voltage with 2.5 volt offset was used for driving. The results in Fig. 5 gives a noise equivalent resolution of 0.01 $^\circ/\text{sec}$. The measured bandwidth is 16.2 Hz. This gives a noise equivalent random angle walk of $0.0025 \text{ }^\circ/\text{sec}/\sqrt{\text{Hz}}$. The output is measured to be linear within 2% for $\pm 20 \text{ }^\circ/\text{sec}$ range.

CONCLUSIONS

In this paper, a single-crystalline micro-gyroscope was fabricated on a single wafer for the first time. The SBM process and the newly developed triple film isolation method were used. The fabricated micro-gyroscope has a noise equivalent random angle walk of $0.0025 \text{ }^\circ/\text{sec}/\sqrt{\text{Hz}}$, which is the lowest in any reported silicon gyroscopes to date.

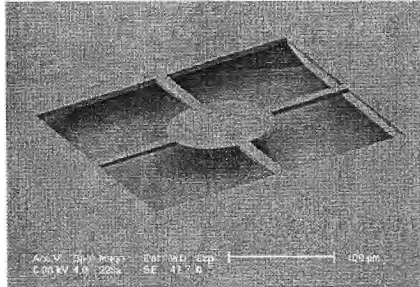
REFERENCES

1. Diem, M.T. Delaye, F. Michel, S. Renard, and G. Delapierre, "SOI (SIMOX) as a substrate for surface micromachining of single crystalline silicon sensors and actuators," *Tech. Dig. Transducers'93*, Yokohama, Japan, June 1993, pp. 233-236.
2. Geiger, B. Folkmer, J. Merz, H. Sandmaier, and W. Lang, "A new silicon rate gyroscope," *Proc. IEEE MEMS'98*, Heidelberg, Germany, Feb. 1998, pp. 615-620.
3. S. Baek, Y. S. Oh, B. J. Ha, S. D. An, B. H. An, H. Song, and C. M. Song, "A symmetrical z-axis gyroscope with a high aspect ratio using simple and new process," *Proc. IEEE MEMS'99*, Orlando, FL, Jan. 1999, pp. 612-617.
4. S. Lee, S. Park, and D. Cho, "The surface/bulk micromachining (SBM) process: a new method for fabricating released microelectromechanical systems in single crystal silicon," *IEEE/ASME J. Microelectromech. Syst.*, vol. 8, no. 4, pp. 409-416, Dec. 1999.
5. K. A. Shaw, Z. L. Zhang, and N. C. MacDonald, "SCREAM I: a single mask, single-crystal silicon, reactive ion etching process for

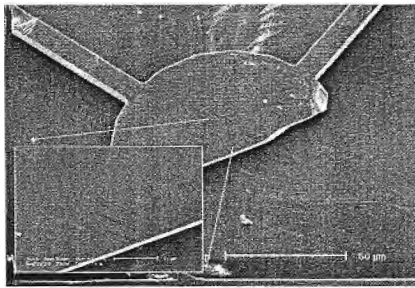
microelectromechanical structures," *Sens. Actuators A*, vol. 40, pp. 63-70, 1994.

6. U. Sridhar et. al., "Trench oxide isolated single crystal silicon micromachined accelerometer," *Tech. Dig. IEDM'98*, San Francisco, CA, Dec. 6-9, 1998, pp. 475-478.

7. S. Lee, S. Park, and D. Cho, "Surface/bulk micromachining (SBM) process and deep trench oxide isolation method for MEMS," *Tech. Dig. IEDM'99*, Washington, D.C., Dec. 1999, pp. 701-704.

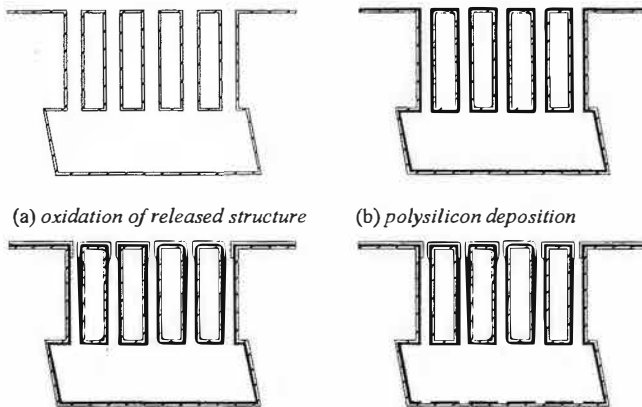


(a) released round plate

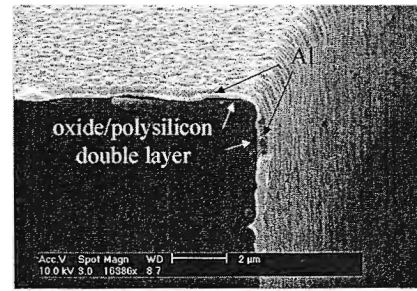


(b) backside of round plate

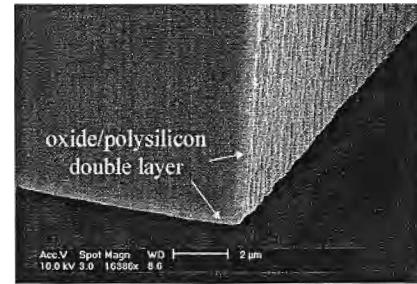
Figure 1. Examples of fabricated structures [7]



(c) metal deposition (d) polysilicon etch for electrical isolation
Figure 2. Process flow of developed isolation method.

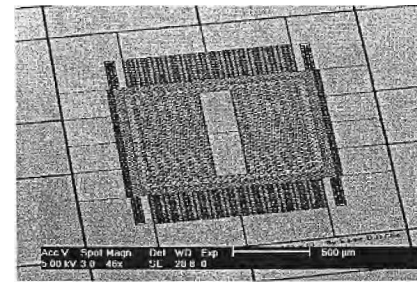


(a) upper part

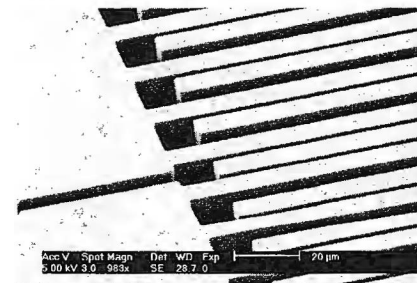


(b) lower part

Figure 3. Electrode processed by the oxide/polysilicon/metal isolation method (40 μm height).



(a) overall view



(b) close-up view of combs

Figure 4. Fabricated micro-gyroscope using the SBM process (40 μm height, 50 μm sacrificial gap)

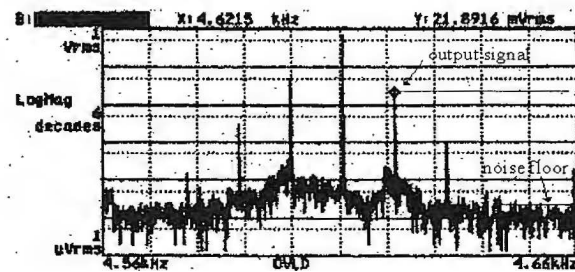


Figure 5. Output Signal of fabricated micro-gyroscope in frequency domain

DEVELOPMENT OF A MAGNETIC FLEXIBLE MEMBRANE MICROPUMP

Melvin Khoo, Liang-Hsuan Lu, and Chang Liu

Department of Electrical and Computer Engineering, University of Illinois at Urbana-Champaign
Urbana, IL 61801-2355

SUMMARY

We present results on the development of a micromachined magnetic membrane pump applicable to integrated microfluidic systems. Structurally, the pump consists of a magnetic micro-actuator and two polymer-based, one-way diffuser valves. The microactuator is based on a 40- μm thick, flexible membrane made of poly dimethyl siloxane (PDMS), a soft silicone elastomer. Membrane displacement is caused by the interaction between an external magnet and ferromagnetic (Permalloy) pieces, embedded within the thickness of the membrane. Pump operation is simple as no precise magnet-to-pump alignment is required. Under an oscillating 1.99×10^5 -A/m external magnetic field, a 0.26- $\mu\text{l}/\text{min}$ flow rate was measured at an actuation frequency of 3.72-Hz.

The core component of the micropump is the magnetic microactuator. We have developed a novel micromachining process for embedding Permalloy pieces within a flexible, suspended PDMS membrane. The dimensions and placement of these Permalloy pieces within the membrane were optimized using computer simulations. Under a 1.84×10^5 -A/m magnetic field, the 2×2 -mm² PDMS membrane achieved a maximum vertical displacement of 211.5- μm .

INTRODUCTION

Micro liquid handling systems [1], in which pumps and valves are key components, have seen great interest during recent years. Actuation principles employed include thermopneumatic, piezoelectric, electrostatic, and electromagnetic. To achieve desirable large membrane displacements, relatively high voltages and high power are needed for these devices. Most membranes use silicon or silicon-based thin films, which have high Young's modulus and are therefore stiff. The maximum displacements of membrane actuators used in pumps and valves are generally limited (tens of microns), whether for flat membranes or even for specially designed membranes with corrugations. This property limits the overall volume flow rate of membrane micropumps.

A new magnetic membrane actuator has been developed. In comparison, the actuator achieves significantly larger membrane displacements than that of typical membrane actuators. This significantly larger displacement is affected by the use of PDMS, which has a Young's modulus 5 orders of magnitude lower than that of silicon. Besides this, PDMS is physically stable and chemically inert, making it more bio-compatible than silicon for biomedical applications. In addition, magnetic actuation is favorable as it provides large and long-range forces.

PRINCIPLE AND DESIGN OF THE PUMP

The micropump consists of two bonded layers (Fig. 1). The microfluidic circuit, Layer I, includes two one-way-flow diffuser valves connected in series with a pump chamber, which is linked by microchannels to the fluid inlet and outlet. The actuation unit, Layer II, is a magnetic membrane microactuator. The diffuser valves in Layer I maximize one-way fluid flow into and out of the pump chamber, in the direction denoted by the arrows. When a

magnetic field is applied, the membrane deflects as shown in Figure 1. This pushes fluid out of the pump chamber through the outlet diffuser. When the external magnetic field is removed, the membrane relaxes and returns to its flat, at-rest position. This draws fluid in through the inlet diffuser to refill the pump chamber.

(A) Membrane Actuator. The structure of the actuator is shown in Figure 2. A thin layer of PDMS rests on top of a silicon cavity. Permalloy pieces, arranged in a parallel order on one side of the membrane, are embedded within the membrane. Interaction between an externally applied magnetic field with the Permalloy pieces causes membrane displacement. The applied field generates magnetic torque in the Permalloy and causes the pieces to deflect, thereby displacing the membrane as shown in Figure 1. Hence, a net volume displacement, or the stroke volume, is produced.

A highly desirable pump characteristic is to achieve the largest possible stroke volume, with a given magnetic field and membrane dimensions. Several unique design issues have been identified and optimized. These key design parameters include: (1) the size of Permalloy pieces, (2) the number of pieces, (3) the size of the membrane, and (4) the placement of Permalloy pieces within the membrane. Finite element analysis optimization simulations using ANSYS yielded the best design layout shown in Fig. 3(a).

(B) Diffuser Valve. The design of our diffuser valves follow the simulation and measurement studies by Olsson *et. al.* [2]. These no-moving-parts diffuser valves have diverging walls in the positive flow direction (Fig. 3b). Diffuser valves used in this pump are shown in Figure 3(b).

FABRICATION

(A) Membrane Actuator. Major steps in the fabrication process are illustrated in Figure 4. Etch holes are opened in the oxide of a silicon wafer. Bulk silicon etching is performed in EDP anisotropic wet silicon etchant until a thin, 30- μm layer of silicon is left (Fig. 4a). A 100- \AA Cr adhesion layer and a 2000- \AA Cu seed layer is then evaporated onto the front surface (Fig. 4b).

A 10- μm thick layer of AZ4620 photoresist is spin-coated on the metals and then patterned for electroplating. Permalloy ($\text{Ni}_{80}\text{Fe}_{20}$) is electroplated over the PR mold to a total height of 22- μm (Fig. 4b). This intentional over-electroplating causes the plated Permalloy to extend laterally over the PR mold edges. The shape of the over-plated structure is shown in Fig. 5. The extension later provides crucial physical restraint to reliably anchor the Permalloy flaps within the membrane when actuated (see Fig. 4e). PDMS (DuPont Sylgard 184) is spin-coated to achieve a 40- μm membrane (Fig. 4c). The PDMS membrane is allowed to reflow to attain a planar top surface.

To release the membrane, the 30- μm silicon layer needs to be removed. Despite the physical stability of PDMS, wet etchants can diffuse through the PDMS membrane at high temperatures (near 100°C) and for extended periods (>1 hour). Direct wafer immersion is therefore undesirable. Hence, we constructed a PDMS protective mold around the wafer for single-sided etching, leaving only the back window open (Fig. 4d). To avoid membrane damage due to strong PDMS-PDMS adhesion between membrane and mold (which causes membrane peel-off during mold removal), a thin, reusable spacer is used. A 1-mm thick PDMS piece,

entirely coated with 540-Å thick Cr acts as this spacer (Fig. 4d). After the silicon window is etched through in KOH, the PDMS mold is carefully removed to release the device (Fig. 4e).

(B) Diffuser Valve. The diffuser valves, pump chamber, microchannels (150-μm wide), and fluid inlet and outlet are defined onto a 175-μm thick layer of SU-8 epoxy-based negative photoresist. PDMS molding produces Layer I in Figure 1.

MEASUREMENTS AND RESULTS

(A) Membrane Actuator. Preliminary experiments have been conducted to relate membrane displacements to the applied magnetic fields. Using a NdFeB permanent magnet (with a maximum surface magnetic field strength of 2.15×10^5 -A/m) as the actuation source, deflections were measured at each corner of each Permalloy piece using an optical microscope.

Figure 9 shows membrane displacements recorded from successive measurements of the actuator at magnetic field strengths of 1.84×10^5 -A/m, 1.49×10^5 -A/m, 1.09×10^5 -A/m, and 8.01×10^4 -A/m, resulting in maximum displacements of 211.5-μm, 194.5-μm, 157.5-μm, and 118.1-μm, respectively. ANSYS simulations produced a good match, with less than 6% error, between experimental results and theoretical expectations.

(B) Micropump. Flow rate versus frequency of applied field has been measured. Food dye placed over the fluid inlet is driven by an oscillating 1.99×10^5 -A/m external magnetic field. Flow measurements were recorded by observing fluid flow along the microchannels. A flow rate of 0.26-μl/min was measured for a 3.72-Hz pumping frequency. The flow rate is a function of the frequency. Dynamic behavior is currently under study.

CONCLUSIONS

An actuator with a flexible, thin PDMS membrane with embedded magnetic pieces is made for the first time. This actuator is capable of achieving relatively large displacements, on the order of 100 to 200-μm. For this actuator, a novel fabrication technique for embedding ferromagnetic material within the thin PDMS membrane has been developed. In addition, design optimizations of the membrane actuator were completed using finite element analysis. The resultant magnetic membrane micropump is readily applicable to remotely-operated, implanted biomedical micro-fluidic systems. This is because it (i) is capable of telemetric operation without tether wires for power input, and (ii) does not require precise alignment between magnetic field and pump.

REFERENCES

1. M. Elwenspoek, *et. al.*, "Towards integrated microliquid handling systems", *J. Micromech. Microeng.*, 4, 227 (1994).
2. A. Olsson *et. al.*, "Diffuser-element design investigation for valve-less pumps", *Sensors & Actuators*, A57, 137 (1996).

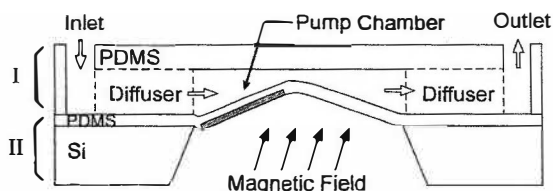


Figure 1. Cross section of assembled micropump.

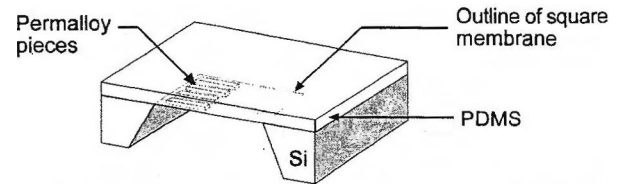


Figure 2. Schematic illustration of the membrane actuator (cut across its symmetry plane to illustrate the cross-section).

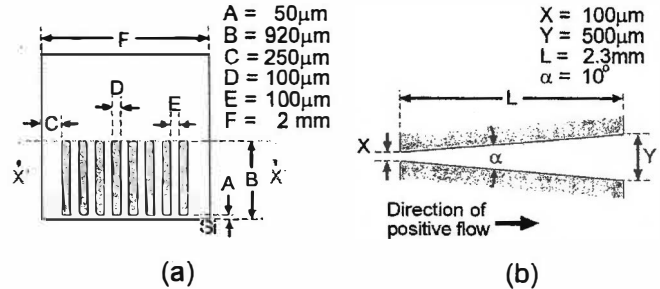


Figure 3. (a) Membrane actuator and (b) diffuser valve layout.

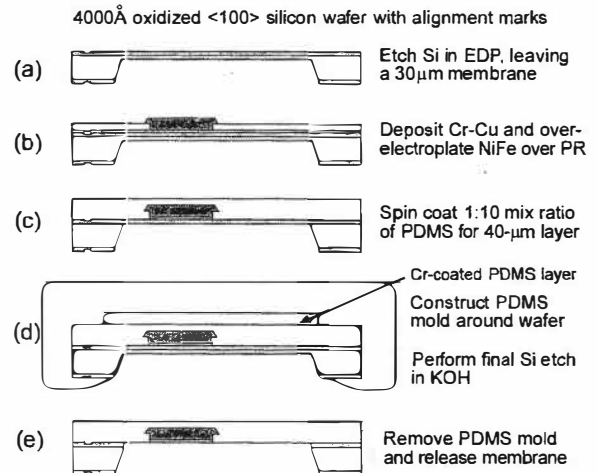


Figure 4. Fabrication process for magnetic membrane actuator.



Figure 5. SEM micrograph showing shape at sides of over-electroplated Permalloy flap.

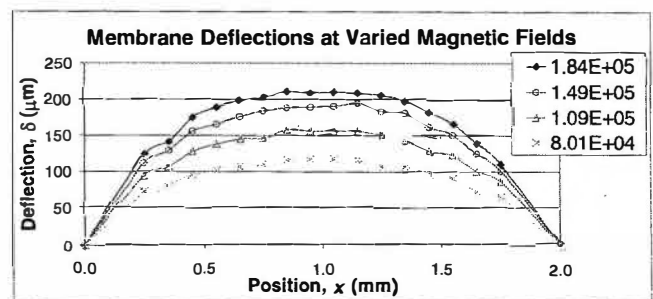


Figure 6. Plot shows vertical membrane displacements along the X'-X' cross-section in Figure 3(a).

100% FOUNDRY COMPATIBLE PACKAGING AND FULL WAFER RELEASE/DIE SEPARATION TECHNIQUE FOR SURFACE MICROMACHINED DEVICES

Andrew D. Oliver¹ and Carolyn M. Matzke²

(1) Electromechanical Engineering and (2) Microsensor R&D Departments
Sandia National Laboratories
Albuquerque, NM 87185

ABSTRACT

A completely foundry compatible chip-scale package for surface micromachines has been successfully demonstrated. A pyrex (Corning 7740) glass cover is placed over the released surface micromachined die and anodically bonded to a planarized polysilicon bonding ring. Electrical feedthroughs for the surface micromachine pass underneath the polysilicon sealing ring. The package has been found to be hermetic with a leak rate of less than 5×10^{-8} atm cm³/s. This technology has applications in the areas of hermetic encapsulation and wafer level release and die separation.

INTRODUCTION

This paper reports the development of a technology that solves two fundamental problems in the area of surface micromachining. These problems are the lack of a small scale hermetic packaging technology and the need to do die level release.

Small scale hermetic packages have received some attention in the MEMS community. Work at the University of Michigan [1-2] and Delphi-Delco [3] among others has demonstrated that small glass on chip packages are both possible and hermetic [2]. However, these processes are either custom foundry processes, not available to outside users, or involve post processing steps on the silicon substrate itself. The work described here uses the released die with the self aligned monolayer anti-stiction coating from the publicly available Sandia National Laboratories SUMMiT IV process [4]. The die is bonded to the machined pyrex lid at 320°C and -1500V with no intermediate steps.

Die level release and handling is also a problem for surface micromachines. Many surface and bulk micromachined devices cannot be diced after the release process and thus cannot be released on a wafer level. This process allows the surface micromachined devices to be released and bonded on a wafer level. After the glass is bonded to the silicon, the packaged devices can be diced without damaging the surface micromachine.

DESIGN

To anodically and hermetically bond glass to silicon, a flat bonding area is required. The bonding area must be flat within 50nm, be large enough for the bond to withstand external loads, and have provisions for electrical leads to traverse beneath or through the bonding area. In this technology, the bonding ring and the electrical feedthroughs are both constructed of polysilicon. The electrical feedthrough is constructed of the poly0 layer that is 0.3µm thick. Next, 2µm of sacrificial oxide (sacox1) is deposited which serves to electrically insulate and mechanically separate the electrical feedthrough from the polysilicon, which is subsequently deposited. The sacox1 layer also serves to hermetically seal the area around the feedthrough. The sacrificial layer is exposed to the release etch at the edge of the bonding region, but because the release etch is of limited duration, less than 60µm of sacrificial oxide is lost on both ends of the feedthrough. This leaves more

than 280µm of oxide to seal the serpentine feedthrough. The poly1, poly2, sacox3, and poly3 layers are deposited above the sacrificial oxide layer and serve to planarize the bonding region. The bonding area is 200µm wide and has a surface area of 3.2×10^{-6} m². A top view of a die with a glass micropackage is shown in Figure 1 and a cross section of the electrical feedthrough is shown in Figure 2.

FABRICATION

This paper reports on an extension of the SUMMiT IV technology which has been discussed previously [4]. One key advantage of the SUMMiT IV process is that the top level of polysilicon is planarized and does not reflect the topology of the underlying layers. For this device, the surface roughness of the bonding surface above the feedthroughs is less than 5nm. This very flat bonding surface reduces the temperature, time and voltage needed to make the seal.

After the wafers are fabricated, released, and coated with an anti-stiction coating, they are placed on the anodic bonding station and bonded. The anti-stiction coating does not appear to effect the bonding and appears to remain both on the bonding surface and on the moving structures after the bonding process. The bonding conditions are a temperature of 320°C, a voltage of -1500V, and a bonding time of five minutes. At the end of the allotted time, the voltage is turned off and the devices are removed from the hot plate.

EXPERIMENTAL RESULTS

One worry throughout this project has been that the electrostatic forces during the anodic bonding process would damage the surface micromachined devices. This problem was minimized by mechanically recessing the inside of the cover by 250µm. This reduces the electrostatic force on the released micromachined parts by a factor of 2500 from a 5µm recess. The comb drives, shown in Figure 3, operated normally after bonding.

The leak rates of the bonded cavities have been measured with a He fine leak detector. The samples were "bombed" with He at a pressure of 3 atmospheres absolute and an exposure time of 2 hours. The samples, which have a volume of 3.6×10^{-3} cm³, were then removed from the pressurized chamber and placed in a chamber connected to a mass spectrometer. Using this system, the He leak rate from the samples was measured for 7 out of 9 samples at less than 5×10^{-8} atm cm³/s. The equivalent standard leak rate in air is less than 1.1×10^{-8} atm cm³/s. Of the two samples that failed, one had a crack across the bonding interface and the second was not fully sealed. The leak rate for the remaining samples is smaller than the resolution of the machine.

Prior to and after the leak checking, some of the samples were diced. The dicing operation did not influence either the mechanical structure of the surface micromachines or their leak rate.

Attempts to characterize the bond strength between the polysilicon and glass were made by separating the glass from the silicon by means of a razor blade. In many places, the glass fractured and remained on the silicon although there was an

isolated instance of a silicon piece remaining attached to the glass. Because the bonding area is only $3.2 \times 10^{-6} \text{ m}^2$, there were also many places where the bond broke at the interface. Interestingly, there did not seem to be a great deal of difference in bond strength between the samples that were supercritically dried and those that were coated with the self aligned monolayer anti-stiction coating. Figure 4 shows a glass fragment on a polysilicon bonding ring sample that was coated with anti-stiction coating before bonding.

CONCLUSION

A hermetic, completely foundry compatible surface micromachine chip-scale package has been developed. The package also allows the surface micromachine to be diced after the release step. A recessed glass cover is placed over the surface micromachined die and anodically bonded to a planarized polysilicon bonding surface. The package leak rate has been measured to be less than $5 \times 10^{-8} \text{ atm cm}^3/\text{s}$ for helium.

ACKNOWLEDGMENTS

The authors would like to thank John McBrayer, Peggy Clewes, Steve Garrett, Kent Schubert, David Plummer, the staff of the Microelectronics Development Lab, Compound Semiconductor Research Lab, and the Electromechanical Engineering Department for their help on this project. Sandia National Laboratories is a multi-program laboratory operated by the Sandia Corporation, a Lockheed Martin Company, for the United States Department of Energy under contract DE-AC04-94AL8500.

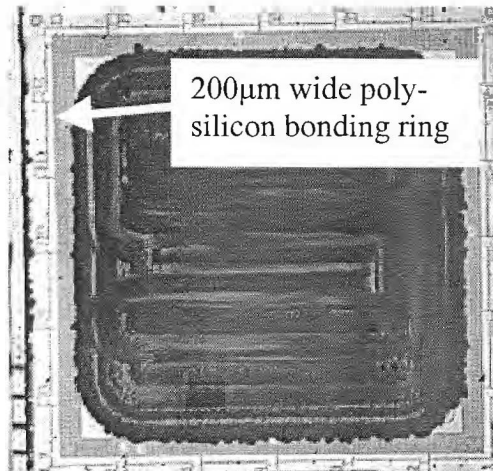


Figure 1. Surface micromachined device with glass cap. The black areas are caused by the surface roughness of the glass where it was milled to create the recess. The die size is 4.6mm x 4.6mm.

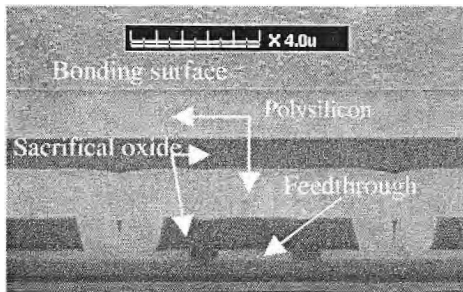


Figure 2. Cross-section of feedthrough. The light gray areas are polysilicon and the dark areas are sacrificial oxide.

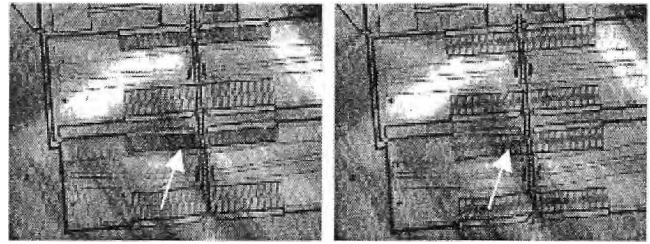


Figure 3. Comb drive operating beneath glass cap. The arrows point out the movement of the comb drives. The fuzzy diagonal lines are artifacts of the machining process used to create the cap.

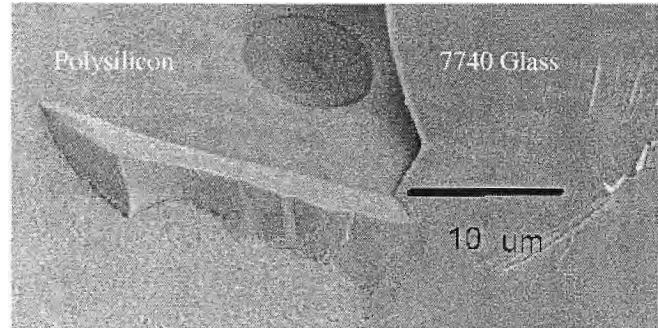


Figure 4. Glass left on polysilicon bonding region after the bond was separated using a razor blade. This sample was supercritically dried. The recess in the top center is an alignment aid.

REFERENCES

1. Y. T. Cheng, L. Lin, and K. Najafi, "Localized Silicon Fusion and Eutectic Bonding for MEMS Fabrication and Packaging", *Journal of Microelectromechanical Systems*, vol. 9, no. 1, pp. 3-8, 2000.
2. B. Ziaie, J. A. von Arx, M. R. Dokmeci, and K. Najafi, "A Hermetic Glass-Silicon Micropackage with High-Density On-Chip Feedthroughs for Sensors and Actuators", *Journal of Microelectromechanical Systems*, vol. 5, no. 3, pp. 166-179, 1996.
3. D. Sparks, D. Slaughter, R. Beni, L. Jordan, M. Chai, D. Rich, J. Johnson, and T. Vas, "Chip-Scale Packaging of a Gyroscope Using Wafer Bonding", *Sensors and Materials*, vol. 11, no. 4, pp. 197-207, 1999.
4. H. Schriener, B. Davies, J. Sniegowski, M. S. Rodgers, J. Allen, and C. Shepard, "Sandia Agile MEMS Prototyping, Layout Tools, Education and Services Program", 2nd International Conference on Engineering Design and Automation, Maui, Hawaii, 1998.

Linearization and Analysis of Electrostatically Actuated MEMS 2D Optical Scanner

Contact: Hiroshi Toshiyoshi
63-128 Engineering IV, Electrical Engineering,
UCLA, Los Angeles, CA 90095-1594
hiroshi@ee.ucla.edu, fax: 310-794-5513

Hiroshi Toshiyoshi, Wibool Piyawattanametha, Cheng Ta Chan, and Ming C. Wu
Electrical Engineering, University of California, Los Angeles

MEMS 2D optical scanners have attracted much attention because of their applications in free-space fiber optic switching matrix [1], projection displays [2], confocal microscopes [3], free-space laser communications, and laser radars. Electrostatic actuation offers many advantages for scanners, including low power consumption, fast response time, and simple drive electronics. However, the electrostatic 2D scanners have highly nonlinear transfer characteristics, which makes control of the scanners difficult. In this paper, we present a linearization scheme that effectively suppress the nonlinearity of electrostatic MEMS 2D scanners. A theoretical model has been developed to predict the linearity of 2D scanner. The simulation results agree very well with experimental data.

Figure 1 shows the SEM of the 2D scanner used in our experiment. It is fabricated by surface-micromachining technique. The micromirror is suspended by two pairs of nested torsion bars (2 μm wide, 200 μm long, and 1.5 μm thick) for X- and Y-scan. To achieve large scan angle, the micromirror (400 μm x 400 μm) is suspended above the substrate with an air gap of 72 μm using the self-assembled micro-elevator structure [4]. The scanning is controlled by quadrant electrodes underneath the micromirror (V_1, V_2, V_3, V_4).

The experimental set-up is shown in Table I(f). A position-sensitive detector (PSD) was used to measure the beam position as a function of the bias voltages. The procedure for calculating the projected beam pattern is outlined in Figure 2. Details of the model will be presented in the conference.

The experimental and calculated scan patterns are summarized in Table 1 for various driving scheme: Column-1 shows the pattern obtained by simply superpositioning the driving voltages V_x and V_y , as described in the table. Due to the large nonlinearity and voltage crosstalk of electrostatic operation, the image is skewed towards the corners by as much as 72% of the scan range (see Table I(a)). The linearization scheme we proposed is shown in Column-2: by pre-biasing the mirror with a DC voltage (V_{bias}) and applying differential voltages ($V_x+V_y, -V_x+V_y, -V_x-V_y, V_x-V_y$) to the quadrant electrodes, the maximum distortion has been dramatically suppressed down to 13.3%. The experimental data (Table I(b)) agrees very well with the simulation results (Table I(e)). Differential voltage operation has been known to improve the linearity of 1D actuators such as a comb-drive mechanism or 1D torsion mirrors. To our knowledge, this is the first report on the linearization of 2D scanners.

We have also studied the effect of mirror shape on the linearity of 2D scanners. We have found that a circular mirror is expected to have the lowest distortion (1.5%), compared to 13.3% for square mirrors. Perfect grid scanning pattern can be obtained by pre-distorting the driving voltages using the data obtained in Table I(b). Distortion as low as 0.33% has been achieved, as shown in Table I(c).

In summary, we have proposed and demonstrated a linearization scheme for electrostatic MEMS 2D optical scanners. We have also studied the effect of mirror shape on the linearity, and found that circular mirror has the lowest distortion.

[1] D. T. Neilson et al., "Fully Provisioned 112x112 Micro-Mechanical Optical Crossconnect with 35.8 Tb/s Demonstrated Capacity," OFC 2000, San Francisco, PD12-1

[2] M.-H Kiang et al., "Actuated Polysilicon Micromirrors for Raster-Scanning Displays," Transducers 97, Chicago.

[3] W. Piyawattanametha et al., "Surface-Micromachined Confocal Scanning Optical Microscope," CLEO 2000 (to be presented)

[4] L. Fan, et al., "Two-Dimensional Optical Scanner with Large Angular Rotation Realized by Self-Assembled Micro-Elevator," IEEE LEOS Summer Topical Meeting on Optical MEMS, 1998, Monterey.

500 words

(1) physical sensors, actuators, or systems

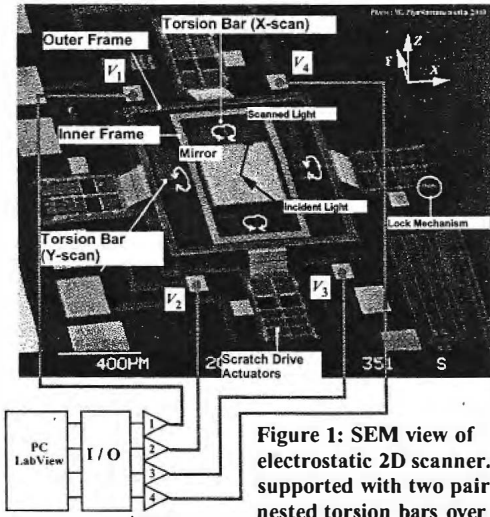


Figure 1: SEM view of electrostatic 2D scanner. Mirror is supported with two pairs of nested torsion bars over the substrate by 72 microns. Driving voltages are controlled by PC and LabView.

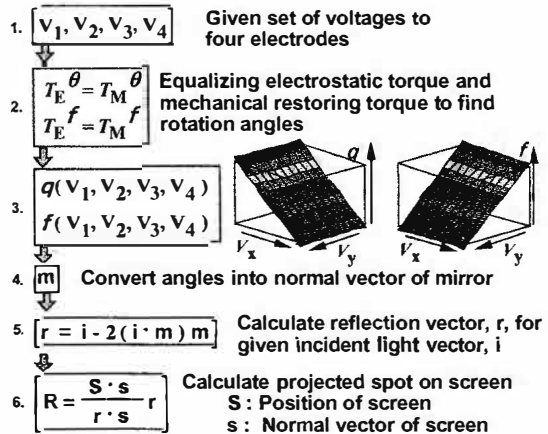


Figure 2: Simulation is programmed to find a position of projected light spot on the screen under a given set of driving voltages.

	Column 1. Non-Differential Operation	Column 2. Differential Operation before Calibration	Column 3. Differential Operation after Calibration
	For scanning the 1st quadrant: $V_1 = V_x + V_y$ $V_2 = V_y$ $V_3 = 0$ $V_4 = V_x$ $V_x = 0 \sim 17 \text{ V}$ $V_y = 0 \sim 34 \text{ V}$	For scanning all of four quadrants: $V_1 = V_{\text{bias}} + V_x + V_y$ $V_2 = V_{\text{bias}} - V_x + V_y$ $V_3 = V_{\text{bias}} - V_x - V_y$ $V_4 = V_{\text{bias}} + V_x - V_y$	$V_{\text{bias}} = 55 \text{ V}$ $V_x = -17 \sim 17 \text{ V}$ $V_y = -34 \sim 34 \text{ V}$
Experiment	(a)	(b)	(c)
Simulation	(d)	(e)	(f) Set up of Optical Experiment & Simulation

Table I: Experimental (upper row) and simulation (lower row) results of scanned grid patterns. As predicted by the simulation, differential voltage operation has been found to be essential for 2D scan of small image distortion. Regular grid patterns can be obtained after calibrating the voltage-angle characteristics.

MICROINSTRUMENT FOR TRANSDERMAL, WOUNDPOTENTIAL MEASUREMENTS

E. V. Mukerjee, S. D. Collins, and R. L. Smith
Micro Instrument and Systems Laboratory (MISL)
Department of Electrical & Computer Engineering
University of California, Davis
Davis, California, 95616

R. R. Isseroff
Department of Dermatology
University of California, Davis
Davis, California, 95616

R. Nuccitelli
Department of Molecular and Cellular Biology
University of California, Davis
Davis, California, 95616

1. ABSTRACT

In vivo animal studies have shown that electrical fields radiate laterally from skin wound sites [1]. In addition, in vitro testing of keratinocytes (the first cellular response to wound healing) has shown cathodally-directed migration in physiological DC electrical fields (100-200 mV/mm) [2]. Results from human wound studies are less forthcoming due to mechanical fragility inherent with standard drawn glass electrode probes. A MEMS alternative was therefore pursued as a reliable, repeatable, wound potential measuring device.

This paper presents the design, fabrication and preliminary testing of an individually addressable, micro-needle array for the measurement of endemic electric fields in wounded tissue. Recording sites are defined by photolithographically patterning thin film Pt electrodes onto a glass substrate, which end in an array of electrical contacts [5]. Aligned anodic bonding of silicon to glass and subsequent dicing with a diamond embedded saw blade create silicon columns attached as an array to both the glass substrate, and the thin film electrodes. The outcome is an array of silicon micro-needles bonded to an electrically insulating glass substrate with Pt electrodes addressing individual needles. Wet chemical etching (HNA) [3,4] sharpens the columns into needles that are sharp enough to pierce skin yet robust enough to withstand multiple penetrations with minimal tip damage (Figure 1). Using a 38.7mV sinusoidal input, an input/output separation distance of 6 inches and a 1 M Ω resistor in parallel, an output signal of 18-20mV was measured by the micro-needle array.

2. METHODS

2.1 Silicon substrate

The needles were fabricated in 4 inch diameter, (100) oriented, p+, silicon wafers. Aluminum was used as a dry etch mask and was deposited onto the polished silicon surface using a CHA Industries electron beam evaporator. Standard photolithography and aluminum etching opened patterns for silicon etching by Reactive Ion Etching (RIE). The patterned aluminum wafer was subsequently etched in a Technics Micro-RIE using sulfur hexafluoride (SF₆) and oxygen (15 and 1.4 sccm, respectively) at 400 watts to a final depth of 18.5 μ m. An orthogonal set of trenches, 150 μ m deep, on 300 μ m centers, was made into the etched surface with a wafer dicing saw (MicroAutomation I006), creating an array of silicon pillars. The aluminum was then removed using a wet etchant (PAN) followed

by a BOE dip to remove any silicon dioxide from the silicon chip surface.

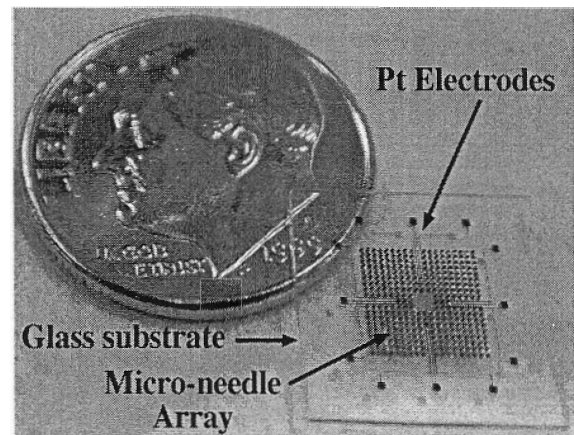


Figure 1. Wound Potential Device

2.2 Glass substrate

Pyrex 7740 glass wafer was used as a platform for the electrodes. Normal photolithographic procedures were used to pattern photoresist on the glass surface as a lift-off mask for the thin film electrode array. The wafer was dipped in a 50:1 HF solution prior to being placed in the CHA Electron beam evaporator (E-beam) for tantalum (Ta) and platinum (Pt) deposition (100 \AA and 500 \AA , respectively). The Pt was then patterned by lift-off of the photoresist in organic solvent.

2.3 Anodic Bonding

The silicon and glass wafers were aligned so as to position the Pt electrodes between the glass and silicon and the contact pads directly beneath the appropriate silicon pillars. Once manually aligned, the bonding cathode was brought down onto the glass surface, adding enough pressure to ensure contact throughout the bonding process. Bonding was performed at 425 $^{\circ}$ C, and 1000V for 1 minute.

2.4 Needle fabrication

The silicon top surface of the bonded pair was coated with photoresist and hard baked for > 1 hour. With the glass side down on the dicing saw, cuts were made in the silicon surface, to a depth of about 350 μ m. This resulted in an array of silicon 3D structures

with a 200 μm square base, and 150 μm tall, on top of which sits a 350 μm tall, silicon, rectangular column with a 100 μm square cross-section. The silicon structures were then etched in "HNA" (1:8:1 hydrofluoric: acetic: nitric acids) until the desired needle shape was obtained. The over baked photoresist on the tops of the columns protected the surface long enough to sharpen them (at which point they fall off) and helped produce needles of uniform height. The chip was then rinsed and oven dried. The needles were then punctured through aluminum foil (~100 μm thick) until the tips of the needles were exposed. The assembly was placed in the E-beam (tips towards the source) for deposition of 100 \AA Ta and 500 \AA Pt. The foil acted as a shadow mask, protecting all underlying structures from metal deposition. The aluminum foil was removed leaving metal only at the tips of the needles. The entire chip was then coated with 1000 \AA of PECVD silicon nitride (Technics) and subsequently etched by an RIE using CF_4/O_2 (15 sccm) and 200 W until the silicon nitride was removed from the tips of the needles [6] (Figure 2).

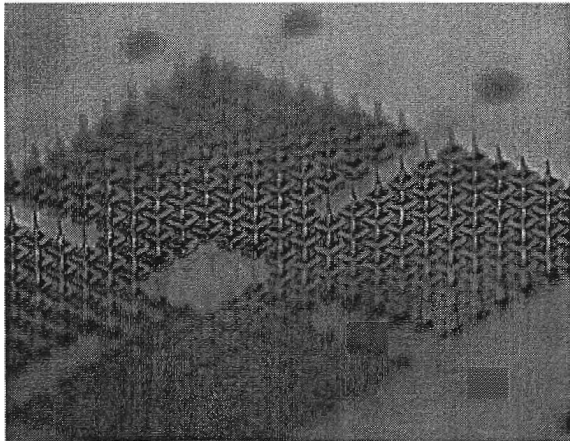


Figure 2. Completed array showing etched silicon micro-needles and electrodes attached to a glass substrate.

3. EXPERIMENTATION AND RESULTS

3.1 Resistance measurements

After the initial bonding and before the second set of dicing cuts were made, contact resistance was measured. A Fluke 8060A Digital Multimeter was used. Three resistance measurements were made: 1) the surface of the silicon --45 Ω 2) the electrical contact pad and the silicon --280 Ω 3) electrical contact pad to another electrical contact pad (using the silicon as the connection between them) --735 Ω .

3.2 In vitro resistance measurements

A saline solution at physiological concentrations was used to test individual addressing and isolation of contacted needles. A stainless steel reference electrode and the tips of the micro-needle array, connected by a Fluke 8060A Digital Multimeter, were placed into the solution and resistance measurements were taken between individual electrodes when their tips were in versus out of the saline solution. Out of solution, the needles were an open circuit (isolation). In the saline, a resistance of 430k Ω was measured.

3.3 In vivo ECG measurements

Using a Medi-Trace 1 S'Offset ECG AgCl as a source electrode, a 38.7 mV sinusoidal signal was introduced into the system. Measurements of the signal were taken by the micro-needle array placed 6 inches from the ECG electrode along the subject's forearm. A 1 M Ω resistor was placed from the micro-needles to ground decrease the current through the subject's tissue. 18-20mV was measured by a single micro-needle. Using the same arrangement, a sub-dermal DC resistance value of 613k Ω was calculated.

4. SUMMARY

Utilizing MEMS technology, a transdermal micro-needle array, with individually addressable needles, was fabricated and bench tested. It was shown that the device has the mechanical strength to puncture the skin and the electrical conductivity to measure both resistance and potential differences both in vitro and in vivo. These measurements lay the groundwork for further testing, specifically the recording of biopotentials related to wound generation and healing.

5. ACKNOWLEDGMENTS

The authors would like to express our gratitude to Dwight Howard for his expertise and on-going technical support throughout the duration of this project.

6. REFERENCES

- [1] D. Inglesia, E. Cragoe, Jr., and J. Vanable, Jr., "Electric field strength and epithelization in the newt (*Notophthalmus viridescens*)", *Journal of Experimental Zoology*, 274 (1996)
- [2] K. Y. Nishimura, R. R. Isseroff, and R. Nuccitelli, "Human keratinocytes migrate to the negative pole in direct current electric fields comparable to those measured in mammalian wounds", *Journal of Cell Science* 109 (1996)
- [3] S. K. Ghandi, VLSI Fabrication Principles-silicon and gallium arsenide, John Wiley and Sons, New York 1994
- [4] P. Campbell, K. Jones, R. Huber, K. Horch, and R. Normann, "A silicon-based, three-dimensional neural interface: manufacturing processes for an intracortical electrode array", *IEEE Transaction on Biomedical Engineering*, 38, 8 (1991)
- [5] S. Tatic-Lucic, J. Ames, B. Boardman, D. McIntyre, P. Jaramillo, L. Starr, and M. Lim, "Bond-quality characterization of silicon-glass anodic bonding", *Sensors and Actuators A* 60 (1997)
- [6] G. Schurmann, P.F. Indermuhle, U. Stauer, and N.F. de Rooij, "Micromachined SPM probes with sub-100 nm feature at tip apex", *Proceedings of the 3rd Conference on Development and Industrial Application of Scanning Probe Methods (SXM-3)*, Basel, Switzerland, 9/16-19 (1998) pp.299-301

THE DESIGN-FIX FOR FIXED-VALVE MICROPUMPS

Christopher J. Morris and Fred K. Forster

Department of Mechanical Engineering, University of Washington
Seattle, WA 98195 USA

INTRODUCTION

The deceptively simple fixed-valve micropump concept has been investigated for over five years for both Tesla-type and diffuser valve geometries [2, 4]. Although some of the first steady-flow experiments indicate the Tesla-type valve has better valve characteristics (higher diodicity), a review of the literature shows the operation of this type of pump is highly dependent on many factors in addition to the valve design, a number of which are still not understood well enough to fully exploit potential applications. Because of the significant potential of this design for 1) handling liquids containing large particles, 2) reliability and 3) scalability, it is important to utilize a rational design approach that investigates all significant parameters affecting performance. While modeling has shown that a high-Q resonant behavior is essential for good performance [1], attempts to predict performance *before* fabrication efforts have not been successful [4]. We present here our latest results in the three critical areas of design: 1) reduced order modeling, 2) mechanical/piezoelectric behavior and 3) valve fluid mechanics. Through careful design it is possible to develop a good-performing pump even with valves that regurgitate 90% of each delivered pump stroke.

MODELING AND ANALYSIS

Reduced Order Modeling: A linear system graph of an entire pump is shown in Fig. 1. It reveals how the electrical input on the left is coupled through the mechanical portion of the system in the middle to the fluid components shown on the right. This representation is utilized for 1) linear analysis of the pump to optimize resonant behavior and 2) nonlinear analysis that includes more complete valve characteristics to predict actual pressure/flow performance. The thirteen parameters shown in Fig. 1 are in turn functions of more parameters related to the geometry and material properties of both the structure and fluid. Yet with the use of finite element structural analysis and fluid dynamic calculations, the only input parameters to the model are those fundamental parameters.

Mechanical/Piezoelectric Behavior: We have recently solved the general problem of optimization of the circular bimorph actuator including a *bonding layer* [3] and have applied the same technique to the case of a square bimorph which we now use for our micropumps, as shown in Fig. 2. This approach utilized the high-level scripting language of ANSYS to perform optimization.

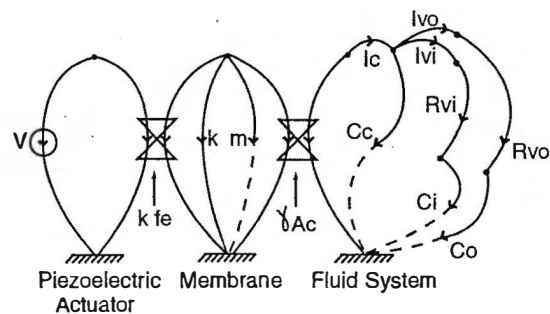


Figure 1. *Reduced-order system model for a fixed valve micropump, with the following symbol definitions: f_e , displacement-per-volt V ; k , spring constant; m , mass; γA_c , membrane shape factor times area; I_c , chamber inductance; C_c , chamber capacitance; I_{vi} and I_{vo} , inlet/outlet valve inductance; R_{vi} and R_{vo} inlet/outlet valve resistance; C_i and C_o , inlet/outlet capacitors.*

The analysis provides accurate values for displacement-per-volt, swept volume and membrane spring constant needed in the reduced order model (see Fig. 3).

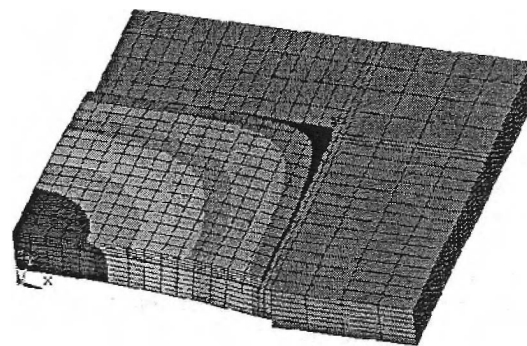


Figure 2. *A three-dimensional finite element model of one-quarter of a square micropump membrane, showing the solution for transverse displacement.*

Valve Fluid Mechanics: Fluid parameters of the valves including resistance R , inductance I , and diodicity are as important as any of the structural parameters. Here we present one important aspect of R and I which has been overlooked in numerous investigations, and can be a major source of error in predicting pump resonant behavior. We have determined that the full transient solution of oscillating viscous flow in the valves is required to properly model valve behavior in terms of hydraulic

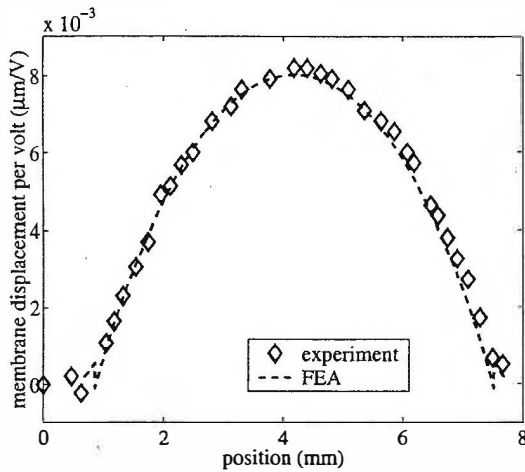


Figure 3. Static displacement-per-volt of a 7mm square pump membrane compared to the FEA model prediction.

impedance $Z = R + i\omega I$. We emphasize this point in this study by presenting results for a simple rectangular duct. The commonly-used expression for R is based on *steady viscous* flow, and the commonly-used expression for I is based on *unsteady inviscid* flow. These expressions lead to a simplified, ad hoc hydraulic impedance Z_s that differs by as much as 30% near the cut-off frequency when compared to the exact impedance Z_e , derived from the Navier-Stokes equations. When applied to a resonant micropump, the ad hoc Z_s led to a prediction that was in error by as much as 300%. This result is shown in Fig. 4 using a chamber/channel system that was similar to a fixed-valve micropump, except that the non-linear valve elements were replaced by straight channels, for which Z_e could be calculated directly. The striking agreement with experiment with simple channels clearly indicates the modeling improvement based on the exact solution.

By applying the exact impedance of a rectangular channel to a channel-segment, series-parallel model of the Tesla-type valve, the resonant behavior of an actual micropump was predicted. This is shown in Fig. 5, along with what the prediction would be without the full viscous solution. Reasonable agreement was obtained, which allows the use of the nonlinear model to optimize net pump output pressure and flow. More recent results indicate that differences seen between experiment and model results in Figs. 5 and 4 can be addressed through computational modeling of the transient flow in the valves.

REFERENCES

- [1] R L Bardell et al. Designing high-performance micropumps based on no-moving-parts valves. In *MEMS*, volume DSC-Vol.62/HTD-Vol.354. ASME IMECE, 1997.
- [2] F K Forster et al. Design, fabrication and testing of fixed-valve micro-pumps. In *ASME Fluids Div.*,

volume 234. ASME IMECE, 1995.

- [3] C. J. Morris and F. K. Forster. Optimization of a circular piezoelectric bimorph for a micropump driver. Accepted for publication in *J. Micromech. Microeng.*, 2000.
- [4] A. Olsson et al. A numerical design study of the valveless diffuser pump using a lumped-mass model. *J. Micromech. Microeng.*, 9, 1999.

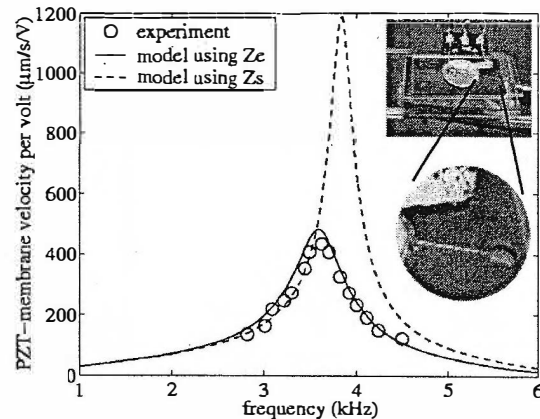


Figure 4. Membrane velocity frequency response of the chamber/channel system shown in the upper right corner, and comparison with model predictions based on simplified and exact impedance, Z_s and Z_e . Shown is good agreement with experiment when the exact form of impedance Z_e is utilized, and over-prediction by 300% for the commonly-used method based on Z_s .

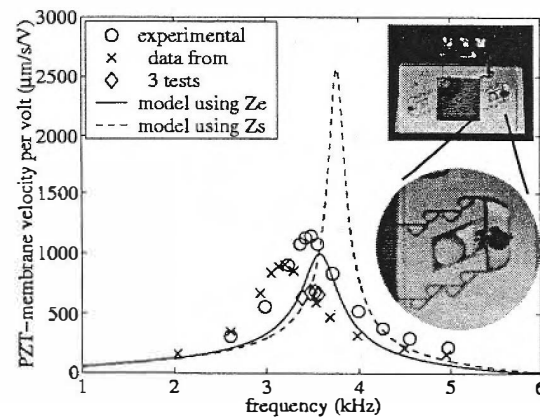


Figure 5. Membrane velocity frequency response of the square-chamber micropump system shown in the upper right corner, and comparison with model predictions based on simplified and exact impedance, Z_s and Z_e . Shown is good agreement with experiment when the exact form of impedance Z_e is utilized, and over-prediction by 300% for the commonly-used method based on Z_s .

NOZZLE-DIFFUSER BASED MICRO BUBBLE PUMP

Jr-Hung Tsai and Liwei Lin*

Mechanical Engineering and Applied Mechanics, University of Michigan

*Mechanical Engineering, University of California at Berkeley

Mechanical Engineering, 5126 Etcheverry Hall, University of California, Berkeley, CA 94720-1740.

Email: jhtsai@engin.umich.edu Phone: (510) 642-8983 Fax: (510) 643-5599

ABSTRACT

A valve-less micropump is demonstrated by utilizing thermal bubbles as the actuation mechanism and a nozzle-diffuser pair as the flow controller. The pump consists of a single resistive heater, a pair of nozzle-diffuser flow controller, and a 1 mm in diameter, 45 μ m in depth pumping chamber. Liquid is pumped by generating and collapsing of thermal bubbles via resistive heating. A maximum flow rate of 5 μ l/min is measured at the driving voltage of 20V with 10% in duty at 250Hz of pulsed power supply.

INTRODUCTION

Micro pumps have wide applications for handling small and precise fluid volumes on chemical, medical, and biomedical devices. Various types of micro pumps have been proposed and demonstrated over the last decade. They can be classified into following types based on the actuation mechanisms: mechanical displacement [1-3], bubble [4], electrohydrodynamic [5], and electrocapillarity [6] pumps. Among them, bubble pumps are less limited by the geometry and size than rotary and diaphragm pumps, also less constrained by the fluid type than electrohydrodynamic and electrocapillarity pumps.

One the other hand, micro valve has been a significant issue in all micropumps because of the relatively high leakage rate [7-10]. Previously, a valve-less pump has been demonstrated with a nozzle-diffuser type flow controller [4] and a diaphragm shape piezoelectric actuator as the pumping mechanism. In this work, instead, bubbles function as a membrane in a diaphragm typed positive displacement pump. Together with the nozzle-diffuser design, this new pump provides advantages of flexible membrane, less dead volume in the pumping chamber and valve-less pumping.

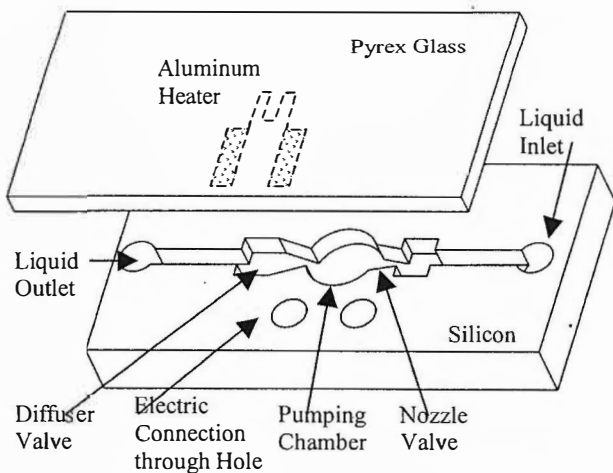


Fig. 1, Schematic drawing of the nozzle-diffuser based bubble pump.

DEVICE FABRICATION

The micropump is schematically drawn in Fig. 1. All the pumping chamber, nozzle-diffuser and channels are fabricated on a silicon substrate at the same depth of 45 μ m. The meander aluminum heater on a Pyrex glass wafer is 10 μ m in width and 1 μ m in thickness. The circular pumping chamber is 1mm in diameter and is connected with a pair of nozzle-diffuser flow controller of 30 μ m in the narrow neck, 274 μ m in the open mouth and 7 $^\circ$ in the diverge angle. The fluid channel is 200 μ m in width. Liquid and electricity connections are constructed by through holes on the silicon substrate. Figure 2 shows the simplified fabrication process flow and the fabricated device. On the silicon substrate, the surface is firstly grown a 1 μ m thick silicon dioxide layer, patterned and etched as the mask of pumping chamber, nozzle-diffuser and channels. A 9 μ m thick photoresist is spun on, patterned and etched by DRIE to open the liquid and electricity interconnection through holes. Afterwards, the photoresist is removed and the silicon wafer is put into DRIE etcher again to define the pumping chamber, valves and channels. After these steps, the silicon wafer is dipped into hydrofluoric acid (HF) to remove silicon dioxide. On the Pyrex glass, the wafer is patterned and etched in buffered HF to form shallow trenches for embedding the aluminum heater for the anodic bonding process. The aluminum layer is then evaporated and patterned by the lift-off process. The silicon and Pyrex wafers are finally aligned and anodically bonded at 380 $^\circ$ C.

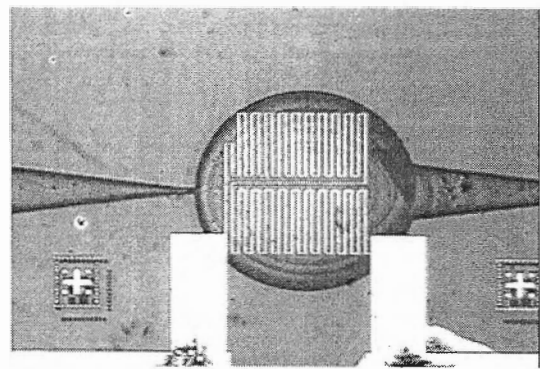
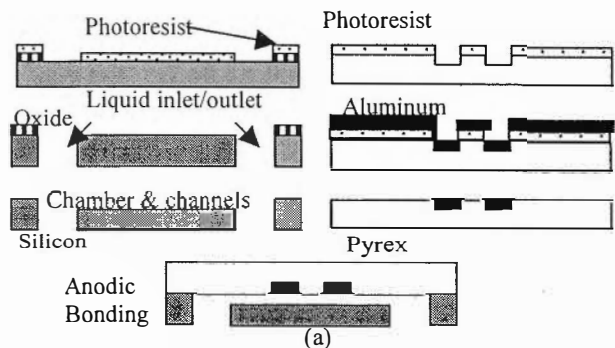


Fig. 2, (a) Simplified fabrication process flow. (b) Optical photograph of the fabricated micropump.

EXPERIMENTS

The pumping flow rate is measured under the same inlet and outlet static pressures. For flow rate measurement, the fabricated micro pump is connected from the inlet and outlet holes to two polyimide tubes of 310 μm in outer diameter and 275 μm in inner diameter. The far ends of the tubes are then connected to syringes filled with liquid as liquid reservoirs. Once the equilibrium state is reached, the pumping flow rate is measured from the averaged speed of the air slug in the tubes.

Figure 3 shows the measured flow rates at three different pulse duties, 5%, 10% and 15%, under pulse voltage of 20 volts. It is found that the maximum pumping rate is 5 $\mu\text{l}/\text{min}$ when the pulse duty is at 10% and the pulse frequency at 250Hz. The pumping effect seems to diminish when pulse frequency is higher than 500Hz. The experiments of pumping rate with respect to pulse width have also been conducted as shown in Fig. 4. The maximum flow rates are found around the pulse width of 0.4 milliseconds at each pulse duties. In experiments, pumping chamber may saturate with gas if the pulse frequencies are outside the peak flow rate region. This gas saturation phenomenon is caused by improper ratio of heating to cooling cycles. Heat residual accumulates on the Pyrex substrate such that generated bubbles cannot condense back to liquid. Consequently, the oscillatory membrane-like pumping effect decreases. On the other hand, if two sequential heating periods are too close, the bubble has no sufficient time to collapse thoroughly. Once the pumping chamber is filled with bubbles, the pumping effect diminishes.

SUMMARY

In the paper, a micro nozzle-diffuser based bubble pump driven by pulse is demonstrated. The pumping volume flow rate is in the order few $\mu\text{l}/\text{min}$. Pulse duty control method is found more effective on the volume flow rate than the pulse frequency control method. Maximum volume flow rate at 5 $\mu\text{l}/\text{min}$ is measured under the conditions of pulse duty at 10% and pulse frequency at 250Hz.

FUTURE WORKS

Although gas saturation can totally hinder the pumping effect, it can be improved and may be prevented by better thermal

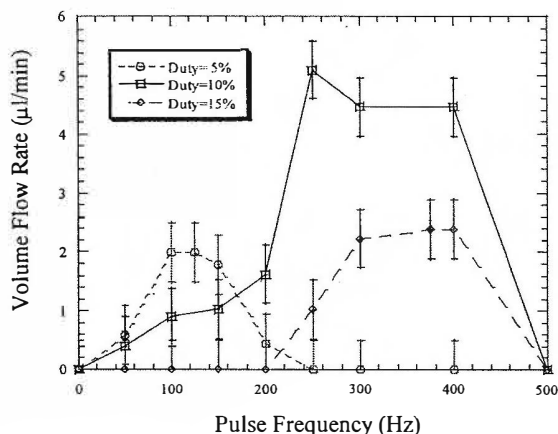


Fig. 3, Volume flow rate measured under the same inlet and outlet static pressure at pulse voltage of 20V.

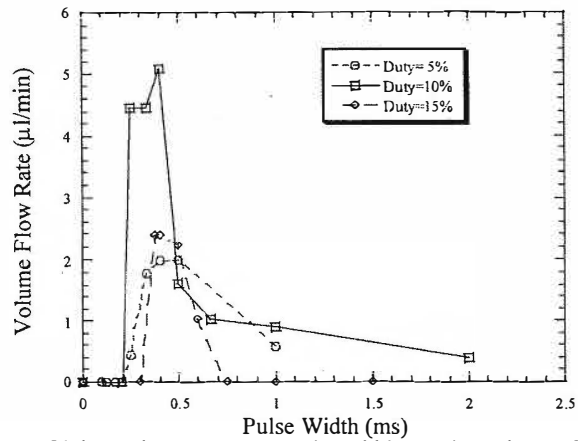


Fig. 4, Volume flow rate versus pulse width at pulse voltage of 20V.

management, such as operating the heater at higher temperature to generate more consistent bubbles, shortening the heating time to prevent heat accumulation on the Pyrex substrate, and widening the heater to generate larger bubble in shorter time. Once the thermal management is improved, the nozzle-diffuser based bubble pump can operate in a more efficient way.

ACKNOWLEDGEMENTS

The authors would thank the Professor Liepmann's research group at UC-Berkeley for the help on testing and discussions.

REFERENCES

1. H. Mizoguchi, M. Ando, T. Mizuno, T. Takagi and N. Nakajima, "Design and Fabrication of Light Driven Micropump," Proceedings of 1992 IEEE Micro Electro Mechanical Systems Workshop, Travemunde, Germany, 1992, pp. 31-36.
2. E. Stemme and G. Stemme, "A Valveless Diffuser/Nozzle-based Fluid Pump," Sensors and Actuators, Vol. A39, 1993, pp. 159-167.
3. B. Bustgens, W. Bacher, W. Menz and W.K. Schomburg, "Micropump Manufactured by Thermoplastic Molding," Proceedings of 1994 IEEE Micro Electro Mechanical Systems Workshop, Oiso, Japan, 1994, pp. 18-21.
4. T. Jun and C.J. Kim, "Microscale Pumping with Traversing Bubbles in Microchannels," IEEE Solid-State Sensor and Actuator Workshop, Hilton Head Island, SC, 1996, pp. 144-147.
5. S.F. Bart, L.S. Tavrow, M. Mehregany and J.H. Lang, "Microfabricated Electrohydrodynamic Pumps," Sensors and Actuators, Vol. A21-23, 1990, pp. 193-197.
6. J. Lee and C.J. Kim, "Liquid Micromotor Driven by Continuous Electrowetting," Proceedings of 1998 IEEE Micro Electro Mechanical Systems Workshop, Heidelberg, Germany, 1998, pp. 538-543.
7. M. Esashi, S. Shoji and A. Nakano, "Normally Closed Microvalve and Micropump Fabricated on a Silicon Wafer," Sensors and Actuators, Vol. A20, 1989, pp. 163-169.
8. E.T. Carlen and C.H. Mastrangelo, "Simple, High Actuation Power, Thermally Activated Paraffin Microactuator," Intl. Conf. On Solid-State Sensors and Actuators (Transducers 99), Japan, 1999, pp. 9.
9. S. Matsumoto, A. Klein and R. Maeda, "Development of Bi-directional Valve-less Micropump for Liquid," Proceedings of 1999 IEEE Micro Electro Mechanical Systems Workshop, Orlando, USA, 1999, pp. 141-146.
10. F. Forster, R.L. Bardell, M.A. Afromowitz, N.R. Sharma and A. Blanchard, "Design, Fabrication and Testing of Fixed-Valve Micropumps," Proceedings of the ASME Fluids Engineering Division, 1995, pp. 39-44.

Ferromagnetic Micromechanical Magnetometers

Jack W. Judy, Henry Yang, Nosang Myung, Pedro Irazoqui-Pastor,
Morton Schwartz, Ken Nobe and Ken Yang

Electrical Engineering Department₁, Biomedical Engineering Department₂,
Chemical Engineering Department₃, of the University of California, Los Angeles
Los Angeles, CA 90095-1594

ABSTRACT

A novel micromechanical magnetometer is introduced that integrates electroplated cobalt-based magnetic materials with surface micromachined polysilicon structures. This new magnetometer has favorable scaling properties (both size and power) when compared to existing magnetic sensing technologies. Theoretical device performance is compared with experimental results with good agreement. These first prototype devices achieve a scale-independent performance of 100 $\mu\text{T} / \text{mrad}$.

INTRODUCTION

We have designed, fabricated, and tested novel low-power ferromagnetic micromechanical magnetometers. The need for miniature high-sensitivity low-power magnetometers is driven by applications such as wireless sensor networks, which are useful for monitoring and controlling large areas, large facilities, and large numbers of mobile assets [1]. Table 1 compares the sensitivity, power consumption, and the scaling properties of the sensitivity with both dimension and power consumption of several magnetometer technologies (adapted from [2]).

Search-coil magnetometers have the advantage of being low power (all power is consumed by sense electronics), but their sensitivity scales down with area, making miniaturization counter productive. Flux-gate magnetometers have a high sensitivity, but it also scales down rapidly as it is miniaturized. Although semiconductor-based magnetometers, such as Hall plates, magnetotransistors, and magnetodiodes, are very compact, the sensitivity of these magnetometers is not competitive.

Table 1. Comparison of magnetometer sensitivity, power consumption, and scaling properties (Adapted from [1]).

Magnetometer	Sensitivity Range (Tesla)	Dimensional Scaling (Sensitivity)	Power Range (W)	Power Scaling (Sensitivity)
Search Coil	10 pT (MHz)	s^{-2}	Limited by sense circuitry	p^0
Flux Gate	100 pT	s^{-2}	$10^{-2} - 10^{-3}$	p^{-1}
Hall Effect	10 μT	s^0	$10^{-3} - 10^{-4}$	$\text{p}^{-1/2}$
Semiconductor	1 μT	s^0	$10^{-3} - 10^{-4}$	$\text{p}^{-1/2}$
MR	10 pT	s^0	$10^{-5} - 10^{-7}$	$\text{p}^{-1/2}$
SQUID	10 fT	s^0	10^1 (cryo)	p^0
MEMS (Resonant)	100 pT	$\text{s}^{-1 \text{ to } -2}$	$10^{-2} - 10^{-5}$	$\text{p}^{-1/2}$
Ferromagnetic MEMS-Based Magnetometer	100 pT*	s^0	Limited by sense circuitry	p^0

*Theoretical performance with circuits designed for inertial microsensors. Magnetoresistance magnetometers have a high sensitivity, but it scales as $\text{p}^{-1/2}$ with power due to a linear dependence on drive

voltage. Although SQUID magnetometers are the most sensitive magnetometers, they require an extensive support system (cryo-refrigeration unit). Recently Lorentz-force based resonant micromechanical magnetometers have been developed that perform well, but suffer from the fact that their sensitivity is scaled down with both dimension and power dissipation (i.e., driving current) and their output is a strong function of Q, thus requiring hermetic packaging [3-4].

The magnetometer that we have designed, fabricated, and tested is a novel MEMS-based magnetometer that is capable of a high sensitivity that does not scale down with dimension and consumes no power other than that needed for the sense circuits.

THEORY

The concept behind the operation of this low-power magnetometer is straightforward: a micromechanical compass. Figure 1 illustrates the basic operation of the MEMS compass. An ambient magnetic field (H) will produce a torque

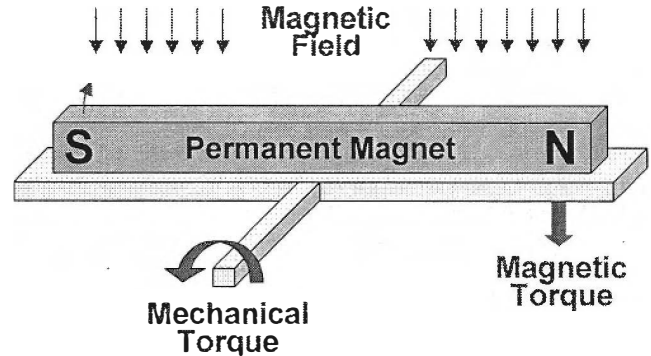


Figure 1. Schematic representation of the principle of operation of the ferromagnetic MEMS magnetometer.

$$T_{mag} = (M \times H) \cdot v \quad (1)$$

on a permanent magnet with a magnetization M . The magnetic torque is then transferred to a torsional microflexure, which creates an equal and opposite mechanical torque

$$T_{mech} = k_{\phi} \cdot \phi \quad (2)$$

with angular deflection ϕ and angular stiffness k_{ϕ} . For a torsion bar with a rectangular cross section, the angular stiffness is proportional to

$$k_{\phi} \sim a^3 \cdot b \cdot G / l \quad (3)$$

with shear modulus G , torsion bar length l , and cross section dimensions a and b where $b \geq a$. By equating Eq. 1 and Eq. 2 the angular deflection can be solved for, which yields

$$\phi = (M \times H) \cdot v / k_{\phi} \quad (4)$$

Despite the fact that the magnetic torque (Eq. 1) scales down with a cubic dependence, so does the angular stiffness of the torsion bar (Eq. 3). The result is that the ratio of the two, and hence the angular deflection produced by the sensed magnetic field, has no dependence on dimensional scaling (Eq. 4).

EXPERIMENTAL DETAILS

Our first prototype devices consist of a polysilicon micromechanical structure, produced with the MUMPS foundry service [5], and a Co-based ferromagnetic film that is electroplated onto the polysilicon plate (Figure 2 illustrates one example). In previous work by our group and others on magnetic microactuators, the electroplated ferromagnetic materials integrated with silicon-based flexures were magnetically soft (i.e., characteristically with a low coercive magnetic field H_c). However, often the best ferromagnetic material for microactuator and microsensor applications is a permanent magnetic material (i.e., characteristically with a high coercive magnetic field). To integrate the cobalt-based magnetic material onto the MUMPS chips, we used the following steps: resist removal, oxide etch to expose polysilicon, adhesion layer (Cr) and seed-layer (Ni) deposition, electroplating mask photolithography, electrically conductive packaging for electroplating, resist removal, seed-layer removal, final release oxide etch, and lastly supercritical drying.

The devices tested consisted of dual $4.2 \times 2 \times 200 \mu\text{m}^3$ polysilicon torsion bars and a $100 \times 100 \times 13.4 \mu\text{m}^3$ ferromagnetic plate. The magnetic properties of the electroplated Co-Ni material have been characterized in both a full-film form, as is typically done, and in the actual geometry tested (i.e., the B-H loop of the $100 \times 100 \times 13.4 \mu\text{m}^3$ Co-Ni plate was measured individually with a vibrating-sample magnetometer to extract the coercivity and remnant magnetization for the theoretical model). The response of these prototype devices to an ac magnetic field was measured with a laser doppler vibrometer. A plot of the angular deflection as a function of magnetic field is given in Figure 3. Although these results clearly demonstrate functionality and feasibility, we anticipate that future devices will integrate capacitive displacement sensing circuits, borrowed from the inertial microsensors industry. The ability to use integrated sense circuitry will provide the opportunity to detect sub-Å displacements, which would translate into detecting a μT -level of magnetic flux with the current device geometry. By improving the remnant magnetization and changing the geometry of the magnet to $100 \times 100 \times 13.4 \mu\text{m}^3$ the magnetometer with integrated sense circuitry could detect a nT-level of magnetic flux.

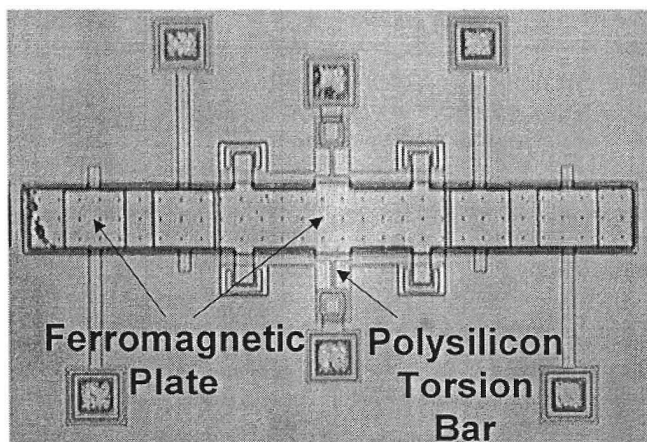


Figure 2. Optical image of a magnetometer with Co-Ni magnetic material electroplated on top of a polysilicon micromechanical structure made with MUMPS [5].

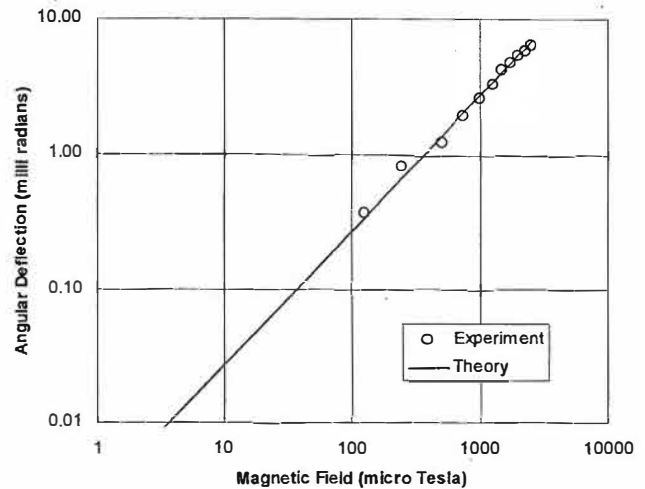


Figure 3. Comparison of experimentally determined angular deflections and theoretical calculations.

CONCLUSIONS

A novel micromechanical magnetometer can be realized by integrating ferromagnetic materials with polysilicon flexures. We have demonstrated the feasibility of this technology by designing, fabricating, and testing prototype devices that achieve a scale-independent performance of $100 \mu\text{T} / \text{mrad}$. We have developed a simple model that adequately predicts out experimental results. By increasing the remnant magnetization, the volume of the magnetic material, and its aspect ratio, a 100-fold improvement in device performance is obtainable. In addition, by using capacitive displacement detection ICs, such as those used in inertial microsensors, a fully integrated MEMS magnetometer could be designed to detect $\sim 100 \text{ pT}$ with less than 1 mW of power.

REFERENCES

1. K. Bult, et. al, "Wireless Integrated Microsensors," *Technical Digest Solid-State Sensor and Actuator Workshop*, (Hilton Head '96), Hilton Head Island, SC, June 1996, pp. 205-210.
2. J. Lenz, "Review of Magnetic Sensors," *Proceedings of the IEEE*, vol. 78, no. 6, pp. 973-989, June 1990.
3. B. Eyre, K.S.J. Pister, and W. Kaiser, "Resonant mechanical magnetic sensor in standard CMOS", *IEEE Electron Device Letters*, vol. 19, (no. 12), pp. 496-498, 1998.
4. D.K. Wickenden, R.B. Givens, R. Osiander, J.L. Champion, D.A. Oursler, T.J. Kistenmacher, "MEMS-based resonating xylophone bar magnetometers", *Proceedings of the SPIE*, vol. 3514, pp. 350-358, 1998.
5. Cronos Integrated Microsystems: <http://www.memrsu.com/>.
6. Jack W. Judy, Richard. S. Muller, and Hans. H. Zappe, "Magnetic microactuation of polysilicon flexure structures," *IEEE Journal of Microelectromechanical Systems*, vol. 4, no. 4, pp. 162-169, 1995.
7. Jack W. Judy and Richard. S. Muller, "Magnetic microactuation of torsional polysilicon structures," *Sensors and Actuators (Physical A)*, vol. 53, no. 1-3, pp. 392-397, 1996.
8. Jack. W. Judy and Richard. S. Muller, "Magnetically Actuated, Addressable Microstructures" *IEEE Journal of Microelectromechanical Systems*, vol. 6, no. 3, pp. 249-256, 1997.

A MEMS 2-D Scanner with Bonded Single-Crystalline Honeycomb Micromirror

Pamela R. Patterson, Guo-Dung J. Su, Hiroshi Toshiyoshi, Ming C. Wu

Electrical Engineering Department, University of California, Los Angeles
Los Angeles, Ca 90095-1594

ABSTRACT

We report on the fabrication and performance of a surface-micromachined 2-D scanner with bonded single-crystalline honeycomb micromirror. The silicon honeycomb is derived from silicon on insulator (SOI) and resolves curvature problems seen in thin film polysilicon mirrors, without incurring the mass increase of a solid silicon structure. Honeycomb micromirrors with surface roughness of <12 nm and curvature of 143 cm have been demonstrated. The 2D scanner is electrostatically actuated and has a mechanical scan angle of 6°. Optical performance of the bonded honeycomb micromirror is comparable to that of solid silicon mirrors.

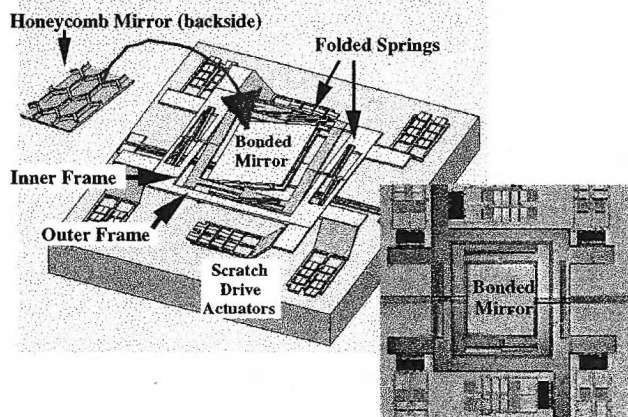


Figure 1. Schematic rendering and photograph of polysilicon 2D scanner with bonded silicon honeycomb mirror.

INTRODUCTION

Fast steering mirrors are used in many applications, including display, switching, sensing, and optical data storage [1]. Surface-micromachining technology paves the way for the design and fabrication of compact, lightweight scanners in a production mode similar to the planar processing of integrated circuits. However, surface-micromachined structures, i.e., released thin films, are extremely sensitive to residual stress and stress gradient, as can be seen in the significant curvature of standard polysilicon micromirrors [2]. This curvature degrades the resolution of the scanning micromirror.

Several approaches have been proposed to reduce the curvature of micromirrors [3]. We have recently reported on a surface-micromachined 2-D scanner with a flat, smooth, single crystalline micromirror formed from SOI [4]. This approach is compatible with the standard surface-micromachining process. While this device shows orders of magnitude improvement in optical properties, the mass of the scanner is increased. To maximize the resonant frequency, a reduction of the total mass is desirable.

In this paper, we report on the successful fabrication of a 2-D scanner with an optically flat, lightweight, honeycomb micromirror. The honeycomb core is a well know structural element for optimization of lightweight and strength. Micro-honeycombs have been used as molds for MEMS structures [5,6]. We employ deep reactive ion etching (DRIE) and wafer bonding techniques to fabricate single-crystalline honeycomb micromirrors. Smooth mirror surface (11.5 nm) and large radius of curvature (143 cm) are achieved. The 2-D scanner has a mechanical scan angle of 6°.

DESIGN AND FABRICATION

The schematic and photograph of the 2-D scanner with honeycomb micromirror are shown in Fig. 1. The electrostatic actuators of the scanner are fabricated by standard polysilicon surface-micromachining process (MUMPs) [7]. The honeycomb mirrors are formed on SOI wafers with 23- μm -thick top layers. The SOI substrates were first thinned down to 200 μm by mechanical lapping. The honeycomb pattern (hexagonal cells with 100- μm -long sides and 10- μm -thick walls) was etched into the top surface silicon using DRIE. The etch was stopped before reaching the buried oxide layer such that a faceplate of silicon remained. After formation of the honeycomb structure, the SOI wafer was bonded to the actuator wafer with patterned photoresist as adhesive in a vacuum oven at 140°C. The SOI substrate was subsequently removed by DRIE etch with the oxide layer providing an etch stop. The oxide was removed in an HF solution prior to honeycomb mirror alignment and patterning. The honeycomb mirrors with 450 μm x 450 μm areas were aligned to the polysilicon actuators by photolithography and etched using DRIE. The exposed photoresist was removed in oxygen plasma. A hard bake at 230°C was done before release of the polysilicon scanner in 49%HF. Finally, the bonded scanning mirror was assembled and raised to 84 μm above the substrate using the on-chip actuators [7].

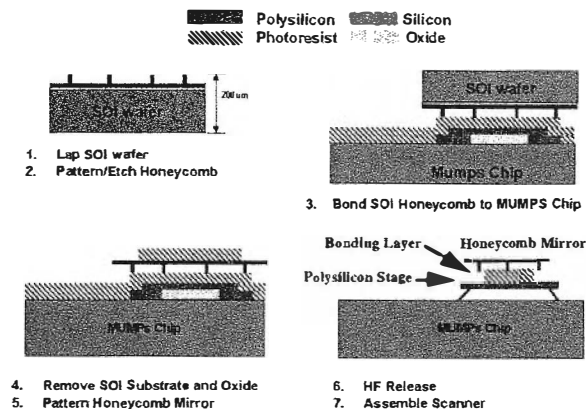


Figure 2. Fabrication process flow

MEASUREMENT RESULTS AND DISCUSSION

The etched profiles of the honeycomb structures are shown in Figure 3 for two different etched depths. The measurements were made using a WYKO RTS 500 surface profiler. Honeycomb samples with faceplate thickness of 1.3, 9, and 12 μm have been made.

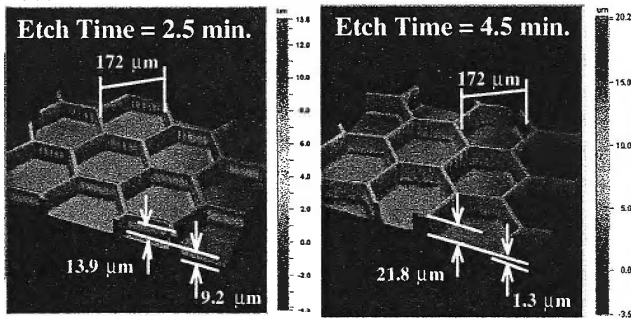


Figure 3. Honeycomb-etched SOI showing depth vs. DRIE etch time

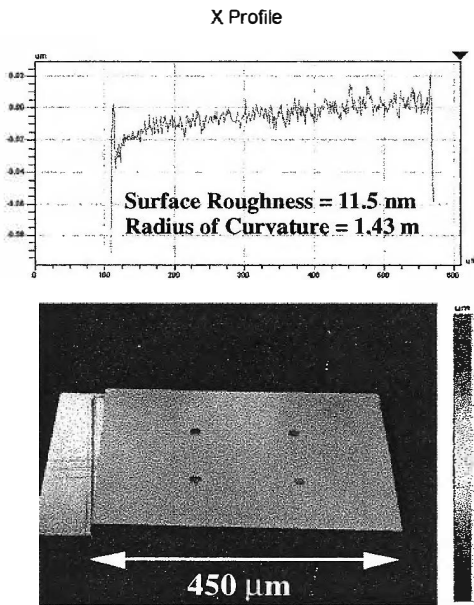


Figure 4. Cross section profile and 3D plot of bonded honeycomb mirror

We have also measured the surface quality of the bonded honeycomb mirrors. The surface roughness values are 123, 12, and 11 nm for honeycomb micromirrors with faceplate thickness of 1.3, 9, and 12 μm , respectively. The corrugation seen in the 1.3- μm -thick sample is most likely due to the current bonding process. We are working on alternative methods that will allow us to realize a smooth surface, for faceplate thickness to $\sim 1 \mu\text{m}$. It should be noted that even with the current corrugation, the surface roughness is still less than $\lambda/10$ at 1.55 μm wavelength, which is sufficient for most applications.

Far Field images of reflected light were measured with a collimated He-Ne laser on the 9 μm sample. This image is essentially identical to the reference wafer, and is significantly improved from the polysilicon micromirrors. The WYKO measurements for the bonded mirror with a 12 μm faceplate show

the mirror is flat with a large radius of curvature (143 cm). The transfer characteristics of the scanner is measured with a Polytech laser Doppler vibrometer. The mechanical scan angle was found to be 6° at 50V.

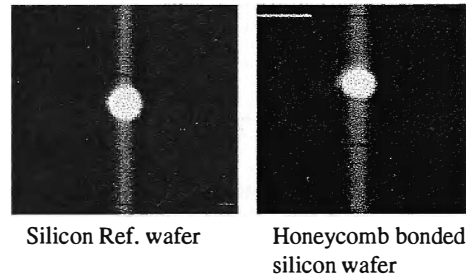


Figure 5. Far field images of reflected He-Ne laser light

CONCLUSION

We have proposed and demonstrated a new technique to fabricate flat, lightweight honeycomb micromirrors for surface-micromachined 2-D scanners. Honeycomb micromirrors with surface roughness $< 12 \text{ nm}$ and a radius of curvature of 143 cm have been demonstrated. 2-D optical scanners with 12° optical scan angle and diffraction-limited optical performance have been achieved.

ACKNOWLEDGEMENTS

The authors would like to thank Allan Hui and Hung Nguyen for technical assistance. The project is supported in part by DARPA.

REFERENCES

1. Muller, R.S.; Lau, K.Y., "Surface-micromachined microoptical elements and systems," Proc. IEEE, vol. 86, p.1705, 1998.
2. R.A. Conant, P.M. Hagelin, U. Krishnamoorthy, O. Solgaard, K.Y. Lau, R.S. Muller, "A full-motion video display using micromachined scanning micromirrors," Proc. Transducers '99, Sendai, Japan, June 1999, pp. 376-379.
3. J. Nee, R. Conant, M. Hart, R. Muller, K. Lau, "Stretched-film micromirrors for improved optical flatness," MEMS 2000, pp. 704-709.
4. G. J. Su, H. Nguyen, P. Patterson, H. Toshiyoshi and M.C.Wu, "Surface-Micromachined 2D Optical Scanners with High-Performance Single-Crystalline Silicon Micromirrors", to be published in CLEO 2000.
5. W.Ehrfeld, P.Bley, F.Gotz, P. Hagemann, A.Maner, J. Mohr, H.O.Moser,D.Munchmeyer,W.Schelb,D.Schmidt,E.W.Baker, "Fabrication of Microstructures using the Liga Process", Proc. IEEE Micro Robots and Teleoperators Workshop, Hyannis, MA, November 1987, pp.11/1-11/11.
6. C. Keller, and M. Ferrari, "Milli-Scale Polysilicon Structures", 1994 Solid-State Sensor and Actuator Workshop, Hilton Head, pp. 132-137.
7. L. Fan, M. Wu, K. Choquette, and M. Crawford, "Self-assembled microactuated XYZ stages for optical scanning and alignment", Transducers '97, pp. 319-322.

A MICROMACHINED RESONANT MAGNETIC FIELD SENSOR

Thierry C. Leïchlé, Martin von Arx and Mark G. Allen
School of Electrical and Computer Engineering
Georgia Institute of Technology
Atlanta, GA 30332-0250
E-mail: leichle@atlas.mirc.gatech.edu; Fax: (404) 894-2776

The measurement of the direction and amplitude of magnetic fields is widely used in many applications. A variety of micromachined structures have been developed to perform this sensing function, including Hall-effect devices and fluxgate magnetometers. In general, there is a tradeoff between power consumption and sensitivity of these devices. For example, micromachined fluxgate magnetometers capable of measuring the direction of the magnetic field of the earth (e.g., 'micromachined compasses') require power consumption levels that are prohibitive for low power, portable applications such as watches.

The work presented here focuses on a resonant approach to the sensing of magnetic field amplitude and/or direction. The motivation for this approach is twofold: (1) resonant structures can be fabricated that require very little actuation power; and (2) the resonant frequency of the structure can be made exquisitely sensitive to small stresses, e.g., the stress caused by the interaction of an external magnetic field with the structure. A typical resonator structure consists of a freestanding plate attached to two anchor pads by means of two beams. It is excited electrostatically by applying an AC, superposed with a DC, voltage between the plate and a bottom electrode located on the substrate. The resonant frequency of the system shifts when a magnetic field is applied. The interaction between the applied field and the magnetization induced in the material causes a change in the stiffness of the beams, thereby changing the resonant frequency of the device.

As an illustration of this concept, a simple device has been designed, fabricated, and tested. The fabrication of the device is based on conventional UV photolithography, micromolding and electroplating of ferromagnetic alloys. The fabrication sequence is shown in Figure 1. It starts with the deposition of a 300 Å titanium / 2000 Å aluminum layer on a glass substrate. This metal layer is patterned using photolithography and wet-etched to create the bottom electrode. An insulator (10 µm of PI2611 polyimide) is then spun and cured on top of the electrodes. A seed-layer of 200 Å titanium / 3000 Å copper is evaporated on top of the polymer. Photoresist (AZ 4620) is then spun and processed in order to create a 30 µm thick mold. A 5 µm thick copper layer is first electrodeposited in the mold as a sacrificial layer. A 20µm thick nickel (80%) - iron (20%) magnetic alloy is electroplated on top of the copper to create the resonating structure. The photoresist mold

is dissolved and the copper sacrificial layer is then selectively and isotropically removed. Since the pads and anchors of the device are larger than the support beams or the resonating portion, no patterning of the sacrificial layer is required as long as the wet etch is stopped as soon as the moving plate is released. The glass substrate is then diced and the devices are individually packaged for testing. Figures 2 and 3 show an optical photomicrograph and a scanning electron micrograph of completed devices, respectively.

Functional devices have been successfully fabricated and tested. The device has been tested in open loop in order to determine the natural resonance frequency (typically on the order of 1 kHz). The device has been placed inside an electromagnet that generated the magnetic field in the plane of the resonator. Since the as-fabricated device was a one-port resonator, the two electrodes have been used to excite the resonator as well as to detect the resonant frequency by measuring the capacitance change between the excitation plates as a function of frequency. A gain-phase analyzer generated the signal that was applied, after amplification, to the resonator. Assessment of the frequency dependence of the magnitude and phase of the resultant displacement current by means of the gain-phase analyzer provided the sensor resonant frequency. This resonant frequency was then measured as a function of incident magnetic field amplitude and direction.

Figure 4 shows the variation of the resonant frequency of the device (in Hz) as a function of the applied magnetic field (in Oersted) when the direction of the field is parallel to the plate. As expected, due to the symmetry of the device an absolute-value type response is seen, with minimum resonant frequency at the point of zero applied magnetic field. Resolutions of 20 Oersted in amplitude of the field have been achieved. The dependence of the resonant frequency on rotation angle between applied magnetic field and the device was also studied, and is given in Figure 5 for a magnetic field excitation of 500 Oersted. An angular resolution of 20° in the direction of the field has been achieved. Although this unoptimized and non-integrated device has not yet proven itself to be of sufficient sensitivity to sense the magnetic field of the earth, the functionality of the sensor has been demonstrated, and the sensing principle should allow for scaling of the sensitivity into this regime without large increases in power consumption.

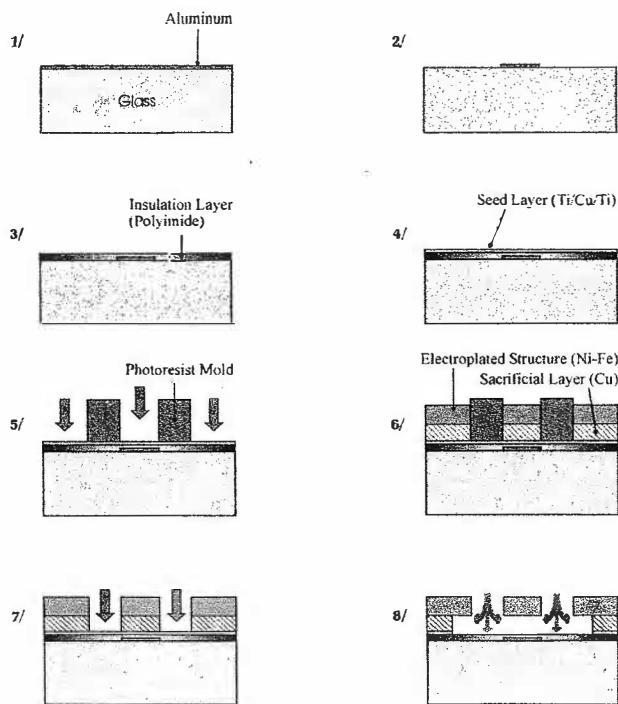


Figure 1. Fabrication Process: 1/Deposition of the aluminum layer; 2/After patterning of the electrode; 3/Insulation of the electrode; 4/Deposition of seed layer; 5/Creation of micro-mold; 6/Electroplating of the sacrificial layer (Cu) and the structure itself (Ni-Fe); 7/Removal of the mold; 8/ Release of the structure by Cu isotropic etch.

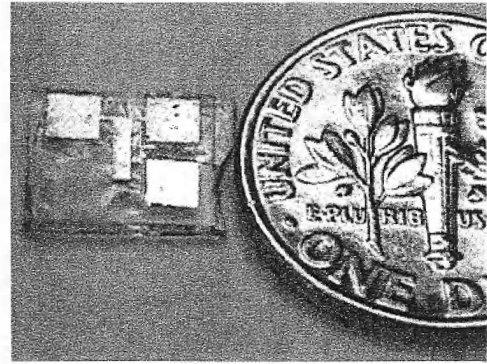


Figure 2. Photograph of a fabricated device and a dime.

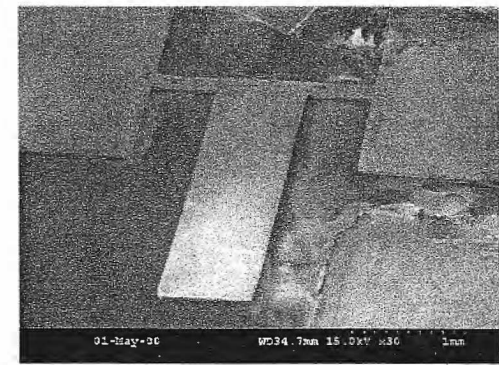


Figure 3. SEM photograph of a fabricated device.

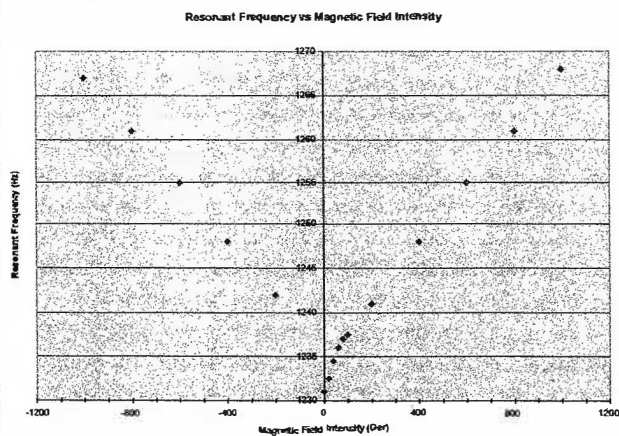


Figure 4. Change of the resonant frequency of the device as a function of the magnetic field intensity (when the direction of the field is parallel to the resonator plate).

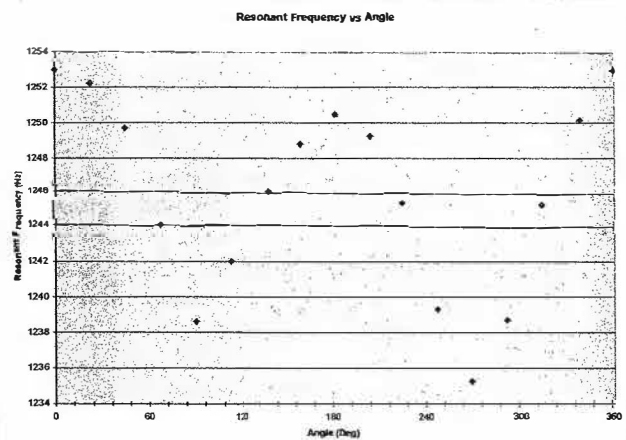


Figure 5. Change of the resonant frequency of the device as a function of the direction of the magnetic field (the intensity of the field is 500 Oersted).

Author Index

Allen, M.	19	Mukerjee, E.V.	9
von Arx, M.	19	Myung, N.	1
Cho, D.	1	Nobe, K.	15
Collins, S.D.	9	Oliver, A.D.	5
Forster, F.K.	11	Park, S.	1
Irazoqui-Pastor, P.	15	Patterson, P.R.	17
Judy, J.W.	15	Schwartz, M.	15
Khoo, M.	3	Smith, R.L.	9
Lee, S.	1	Su, G.-D. J.	17
Leïchlé, T.C.	19	Toshiyoshi, H.	7, 17
Lin, L.	13	Tsai, J.-H.	13
Liu, C.	3	Wu, M.C.	17
Lu, L.-H.	3	Yang, H.	15
Matzke, C.M.	5	Yang, K.	15
Morris, C.J.	11		